Nanoscale

ROYAL SOCIETY OF CHEMISTRY

PAPER

View Article Online
View Journal | View Issue

Check for updates

Cite this: *Nanoscale*, 2026, **18**, 8813

Surface-percolated GNP coatings on 3D-printed PLA lattices for tunable EMI shielding and flame-retardant multifunctionality

Najmeh Taala,[a] Mohammad Aberoumand,[a] Erick Gabriel Ribeiro dos Anjos[a,b] and Uttandaraman Sundararaj *[a]

Received 27th November 2025,
Accepted 16th March 2026

DOI: 10.1039/d5nr05018a

rsc.li/nanoscale

The growing demand for lightweight systems capable of integrating multiple functionalities has accelerated interest in multifunctional material systems (MFMS). This work presents a scalable approach for fabricating such systems by combining 3D-printed porous PLA lattices using the Fused Deposition Modeling (FDM) method at 30% infill, followed by dip-coating of graphene nanoplatelets (GNPs). Up to nine coating cycles were applied to diamond-lattice structures, enabling tunable electromagnetic interference (EMI) shielding, improved flame retardancy, and surface-controlled electrical conductivity. FESEM analysis revealed compact and laminar (platelet-stacked) GNP assemblies, with early cycles producing uniform coverage and later cycles showing increased surface densification. EMI shielding effectiveness (SE_T) across the X-band (8.2–12.4 GHz) increased with coating cycles, reaching ~25 dB after nine cycles. Shielding was absorption-dominated, and a resonance peak near 10–10.5 GHz demonstrated the potential to create frequency-tunable absorption performance using pore geometry. Electrical conductivity increased almost linearly with coating cycles, reaching 10^2 S m^{-1} at nine cycles. Notably, surface-percolating conductive networks emerged after the first cycle—distinct from classical bulk percolation—highlighting the efficiency of surface-enabled charge transport on 3D architectures. Flame-retardant performance also improved significantly: thermogravimetric analysis (TGA) showed a 24.4 °C rise in $T_{d\text{-max}}$ and a 340% increase in char yield, while the Limiting Oxygen Index (LOI) increased from 19.1% (neat PLA) to 27.5% after nine cycles. Surface engineering steps—including NaOH etching and PEI functionalization—enhanced wettability and facilitated uniform GNP deposition, improving strong adhesion, especially at lower coating cycles.

Introduction

Advanced functional polymer materials are gaining increasing attention due to their potential to integrate multiple functionalities into a single, lightweight platform. Multifunctional Material Systems (MFMS) represent a class of engineered materials in which two or more functions—such as electrical conductivity, thermal stability, and mechanical strength—are incorporated within one material system. This eliminates the need to assemble separate monofunctional components, simplifying device architecture and reducing failure points.[1,2] The emergence of MFMS has opened new pathways for improving design flexibility, minimizing assembly complexity, and enhancing system-level reliability—all while enabling weight reduction, sustainability, and cost efficiency. These advantages are particularly crucial in demanding sectors such as defense,[3,4] aerospace,[5] automotive,[6] wearable electronics,[7,8] telecommunications,[9] the Internet of Things (IoT),[10] soft robotics,[11,12] and biomedical devices.[13]

The rapid advancement of telecommunications and digital technologies has led to the widespread presence of electromagnetic (EM) waves—oscillating electric and magnetic fields that are now an integral part of modern environments. These ubiquitous electromagnetic waves can cause electromagnetic interference (EMI) with other electronic devices, adversely affect the performance and reliability of nearby devices.[14–16] Although EMI shields are designed to mitigate interference, reflection-driven secondary scattering can reduce shielding efficiency and contribute to secondary electromagnetic pollution.[17,18] In parallel, potential biological and health risks associated with EM field exposure, from DNA chain breakage to brain tumors, have been studied in the medical/health-science literature, and reported associations continue to be

---

[a] Department of Chemical and Petroleum Engineering, University of Calgary, Calgary, AB T2L1Y6, Canada. E-mail: ut@ucalgary.ca
[b] Department of Science and Technology, Federal University of São Paulo, São José dos Campos, São Paulo, Brazil

discussed depending on exposure conditions and specific biological endpoints.[19–21] As a result, electromagnetic interference (EMI) shielding has become a critical design requirement, particularly for precision electronics and densely packed circuitry. Metals have traditionally been used for EMI shielding due to their high electrical conductivity, which reflects incident EM waves. However, their inherent drawbacks—such as high density, corrosion susceptibility, processing challenges, and reflection-driven secondary EM pollution—limit their utility in next-generation, lightweight devices.[14]

To overcome the limitations of metallic EMI shielding, polymer-based alternatives have been extensively developed over the past two decades. These materials offer distinct advantages, including low density, chemical resistance, ease of processing, and the ability to integrate additional functional properties.[22] In polymer composites and hybrid systems, EMI shielding generally occurs through three main mechanisms: reflection, absorption, and multiple internal reflections.[22,23] Reflection results from the impedance mismatch between the shield and the surrounding environment, where free electrons in the material generate an opposing field to cancel out the external EM wave.[24–26] Absorption, meanwhile, occurs through mechanisms such as Joule heating due to electrical resistance, dipolar polarization, and interfacial polarization at the boundary between two materials with different electrical conductivities.[26–28] Ideally, materials with minimal surface reflection and moderate impedance mismatch are preferred, as they enhance absorption while reducing secondary EM pollution.[28] Multiple internal reflections may contribute to attenuation when the shield's thickness approaches or is below the skin depth, contributing to additional wave attenuation—particularly in porous systems. In this context, architectural factors such as pore geometry, structural periodicity, and lattice resonance can create additional shielding effects not observed in bulk materials.[29] For instance, cavity resonance occurs when EM waves are trapped within a structured cavity, forming standing waves at specific frequencies influenced by the cavity's geometry and size.[30,31] Researchers have explored these effects using 3D printing to design metamaterials with tailored pore sizes and lattice structures to optimize EMI shielding and absorption. One study by Lv *et al.*[32] demonstrated that hexagonal honeycomb lattices combined with small pore sizes significantly improved EMI shielding performance in TPU/CNT composites, with optimal results observed when pore sizes were smaller than approximately one-fifth to one-eighth of the incident wavelength.

Despite their multifunctional potential, polymers are inherently flammable, posing serious safety risks in many applications. Therefore, integrating flame-retardant features into polymer-based MFMS is essential, particularly for environments that require both fire resistance and EMI shielding.[33–37] Aerospace, electronics, and electric vehicles are among the sectors urgently demanding such dual-functionality materials.[38–40] However, traditional flame retardants such as halogenated or borate-based compounds have raised environmental and health concerns.[41,42] In response, carbon-based additives, especially graphene nanoplatelets (GNPs), have emerged as promising, eco-friendly alternatives offering both flame resistance and additional functional benefits.[43]

Graphene nanoplatelets (GNPs) have been shown to enhance flame retardancy in polymers by improving structural stability, increasing char yield, and forming compact, layered barrier structures. Their platelet-like morphology introduces a tortuous pathway for mass transfer, reducing oxygen diffusion and heat penetration.[43–45] Hofmann *et al.*[46] reported a 74% reduction in the peak heat release rate (PHRR) in polypropylene composites with only 5 wt% of functionalized graphene. Huang *et al.*[47] achieved a 46% decrease in PHRR using 8 wt% graphene oxide in EVA. Ali *et al.*[48] demonstrated that combining GNPs with intumescent flame retardants in polypropylene formed a dense char layer, significantly improving flame resistance. Similarly, Idumah *et al.*[49] observed a LOI increase from 15% to 24% in PP composites with only 0.1 phr exfoliated GNP; this value reached 31% with 5 phr.

Beyond blending GNPs into polymers, surface coating has emerged as another effective strategy to enhance flame retardancy with minimal material usage. Matta *et al.*[50] investigated the deposition of graphene nanoplatelet (GNP) inks onto PET foam *via* surface coating techniques. Their findings revealed that coating the foam with a poly (styrene sulfonate)/GNP (PSS/GNP) dispersion, with a GNP loading of 5.3 wt%, significantly delayed flame penetration (1000 °C) from 10 seconds to 210 seconds. Additionally, a lower GNP intake of 3.5 wt% resulted in a 68% reduction in the heat release rate (HRR) compared to uncoated PET foam. Kim *et al.*[51] developed graphene phosphonic acid (GPA) as a flame-retardant coating for traditional Hangi paper. Remarkably, a GPA loading of 13.6 wt% prevented ignition entirely, allowing only the emission of white smoke. Song *et al.*[52] utilized a Meyer-rod coating process to deposit a hybrid film composed of GNP, carbon nanotubes (CNTs), and lignin onto cellulose paper. This approach formed a dense and compact protective layer that effectively inhibited oxygen and decomposition byproduct penetration. As a result, flammability was significantly reduced, and the coated samples exhibited excellent self-extinguishing behavior. Chen *et al.*[53] developed a layer-by-layer coating strategy using graphene oxide functionalized with a phosphorus–nitrogen flame-retardant compound, alternated with polyethyleneimine (PEI) layers. This multilayer coating created a protective barrier on the polyvinyl alcohol (PVA) matrix, substantially reducing heat transfer. Compared to neat PVA, the coated system showed a 30 °C increase in initial decomposition temperature (from 230 °C to 260 °C) and a 60% reduction in total heat release with 30 bilayer cycles.

In the present study, a facile and scalable dip-coating process was employed to deposit GNP ink onto surface-modified, porous PLA structures fabricated *via* 3D printing. The resulting samples, engineered in a diamond-like lattice configuration, exhibited a combined enhancement of multifunctional properties, including electromagnetic interference (EMI) shielding, electrical conductivity, and flame retardancy. The lattice-based architecture enabled by additive manufacturing produces lightweight structures with high surface area, promoting absorption-dominant EMI shielding behavior through increased wave interaction and internal scattering within the porous framework.

Unlike conventional approaches that focus on bulk composites or flat-coated substrates, this work establishes a novel integration of 3D-printed porous architectures with nanomaterial dip-coating, revealing correlations between structural geometry, coating morphology, and adhesion behavior. The combination of engineered porosity and surface chemistry influenced the GNP coating uniformity, adhesion strength, and microstructure formation—revealing how architectural design directly governs surface wetting, layer compaction, and overall multifunctional performance. This structural-materials interaction, particularly the emergence of surface percolation-based conductivity and geometry-dependent EMI shielding tunability, provides insight into designing lightweight, multifunctional systems through surface-enabled phenomena.

Altogether, this study demonstrates a scalable approach that integrates lattice architecture with surface-enabled conductive coatings to achieve absorption-dominant EMI shielding and improved fire performance at low effective GNP loading.

Materials and methods

Materials

Graphene nanoplatelets (GNPs) were obtained in powder form from MGgrafeno® Project (Belo Horizonte, Brazil) with a reported purity of 94%. According to the manufacturer's specifications, the GNPs consist of 6–10 graphene layers, with lateral dimensions of 1–2 μm and an average thickness of approximately 2 nm. All solvents and reagents used were of analytical grade. 2-Propanol (99.5% purity), sodium hydroxide pellets (97% purity), and chloroform (99.8% purity, stabilized with ethanol) were purchased from Sigma-Aldrich (St Louis, MO, USA). Branched polyethyleneimine (PEI) was also obtained from Sigma-Aldrich in viscous liquid form, with a weight-average molecular weight (M_w) of approximately 25 000 g mol^{-1} and a number-average molecular weight (M_n) of ~10 000 g mol^{-1} (determined *via* gel permeation chromatography, GPC). Its density was reported as 1.03 g mL^{-1}. Polyvinylpyrrolidone (PVP), supplied by Sigma-Aldrich in powder form, had a molecular weight (M_w) of approximately 1 300 000 g mol^{-1}. Commercial polylactic acid (PLA) filament for 3D printing was acquired from Shenzhen Creality 3D Technology Co., Ltd (Shenzhen, China), under the trade name "Hyper Series PLA". The filament was white in color, with a diameter of 1.75 mm and a density of 1.23 g cm^{-3}. In addition, PLA pellets were purchased from NatureWorks (Minneapolis, MN, USA), with the same density of 1.23 g cm^{-3}.

Preparation method

3D-printing process. All samples were fabricated using a Sermoon D3 Pro dual-nozzle fused deposition modeling (FDM) 3D printer (Shenzhen Creality 3D Technology Co., Ltd, Shenzhen, China), equipped with a 0.4 mm nozzle. The printing parameters were set to a nozzle temperature of 210 °C, a bed temperature of 60 °C, and a printing speed of 100 mm s^{-1}. A 30% infill density was employed using a line infill pattern oriented at ±45°, and each printed structure included three solid bottom layers.

The diamond lattice architecture was selected as a model geometry due to its geometrical simplicity—uniaxial cross-section, unidirectional 3D printing direction, and simple geometrical characteristics—which allow for repeatable and uniform dip-coating and ink penetration inside the lattice, and indeed its mature and well-practiced 3D printing unit-cell structure. In this study, the printer feedstock filament diameter was 1.75 mm, and the nozzle diameter (the raster filament's diameter) was fixed at 0.4 mm to ensure the lattice resolution. The characteristic pore size (mesh size) was 0.9 mm, corresponding to 30% infill density, to ensure EM waves-structure interaction according to the pore's length scale to the X-band's wavelength (2.5–3.75 cm[54]) proportionality.

For electromagnetic interference (EMI) shielding and contact angle measurements, samples were printed with dimensions of 22 × 11 × 3 mm^3. These prints contained three solid bottom layers but no top layers, allowing for direct surface exposure.

Samples used for Limiting Oxygen Index (LOI) testing were fabricated with dimensions of 60 × 10 × 3 mm^3, following the same printing parameters as the EMI/contact angle specimens. For the tape-peeling adhesion tests, larger square samples (50 × 50 × 3 mm^3) were printed, incorporating both three solid bottom layers and three solid top layers to better simulate coated functional surfaces.

The 3D sliced models corresponding to each test category—EMI shielding, LOI, and tape-peeling—are illustrated in Fig. 1, panels (a), (b), and (c), respectively.

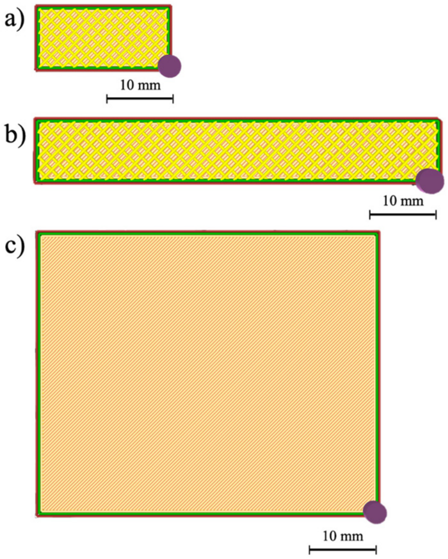

Fig. 1 Sliced 3D-printing visualizations of the sample geometries used for (a) electromagnetic interference (EMI) shielding, (b) limiting oxygen index (LOI) testing, and (c) tape-peeling adhesion tests.

Surface Etching of 3D-Printed PLA Samples. All 3D-printed PLA samples underwent a two-step cleaning procedure to remove residual glue and surface contaminants. First, the samples were immersed in 2-propanol and sonicated for 15 minutes, followed by a second 15-minute sonication in deionized (DI) water. After each step, the samples were gently dried with sterile laboratory tissue.

For surface etching, sodium hydroxide (NaOH) pellets were dissolved in DI water to prepare a 1 M NaOH solution, which was stirred at 400 rpm for 1 hour to ensure complete dissolution. The pre-cleaned PLA samples were then submerged in the 1 M NaOH bath for 1 hour and 45 minutes, a duration chosen to achieve effective surface modification without compromising structural integrity. This etching treatment increased surface roughness—enhancing mechanical interlocking capacity while preserving the dimensional stability of the 3D-printed lattice. The selected etching time was considered near-optimal, producing a roughened surface without excessive polymer degradation.[55]

The etching mechanism is dominated by hydrolytic degradation, in which NaOH attacks and cleaves ester bonds within the PLA backbone, generating both chemical and topographical modifications at the surface.[56,57] After etching, samples were thoroughly rinsed with DI water to remove any residual NaOH and reaction byproducts, ensuring a neutral, clean surface before proceeding to functionalization.

Post-etching surface functionalization of PLA samples. Surface functionalization was performed by immersing the etched PLA samples in a 2 wt% polyethyleneimine (PEI) solution. PEI was first dissolved in DI water and stirred at 400 rpm for 2 hours to achieve complete mixing. The etched PLA samples were then submerged in the PEI solution for 60 minutes, enabling the introduction of amine ($-NH_2$) functional groups onto the PLA surface.

This functionalization step served two key purposes:

(1) to counteract the increased hydrophobicity induced by NaOH-etching-induced roughness, and

(2) to introduce chemically active sites capable of anchoring graphene nanoplatelets (GNPs).

PEI, being a polycationic polymer rich in amine groups, interacts strongly with the hydroxyl (–OH) and carboxyl (–COOH) functionalities formed during NaOH etching, contributing to improved interfacial adhesion.[58] Moreover, PEI acts as an effective molecular bridge between the PLA surface and GNP coatings, enhancing bonding through electrostatic attraction and hydrogen bonding with GNPs dispersed in the dip-coating ink.[59–61]

Following functionalization, the samples were rinsed with DI water to remove any loosely adsorbed PEI molecules. A mild thermal curing step at 50 °C for 15–20 minutes in a convection oven was then applied to remove residual moisture and promote molecular rearrangement within the PEI layer. This curing process further strengthened hydrogen bonding and electrostatic interactions, resulting in a more robust PEI–PLA interface.[62]

Dip-coating ink preparation. Polyvinylpyrrolidone (PVP) was first dissolved in 2-propanol (2.5 wt%) under magnetic stirring at 400 rpm for 1 h. PVP served as a stabilizing agent to facilitate uniform dispersion of graphene nanoplatelets (GNPs) in the solvent. Commercially supplied GNPs were then added at a concentration of 5 wt%, and the mixture was stirred for 24 h at 400 rpm to promote homogeneous dispersion.

To further reduce agglomeration, the suspension was subjected to bath sonication for two 15 min cycles with a 15 min interval to prevent excessive heating. During dip coating, the dispersion was maintained under continuous stirring (400 rpm) and sealed to minimize solvent evaporation and preserve ink stability.

Dip-coating procedure. For the dip-coating process, surface-functionalized 3D-printed PLA samples were held vertically by their shorter edge using tweezers and quickly immersed in the GNP ink for one minute. Each sample was then withdrawn perpendicularly to minimize flow irregularities.

After each coating cycle, the samples were placed in a convection oven at 50 °C for 20 minutes to allow complete solvent evaporation before the next cycle was initiated. The number of coating cycles ranged from 1 to 9, and samples coated at cycles 0 (uncoated), 3, 6, and 9 were selected as representative groups for characterization. These were labelled as "cycle 0", "cycle 3", "cycle 6", and "cycle 9", respectively, as shown in Fig. 2. All samples featured a one-sided structure and were fully coated throughout the accessible lattice structure. The term "one-sided structure" refers to the geometric asymmetry of the printed lattice, in which one face is capped by a solid wall, while the opposite face remains open to the porous diamond lattice. This architectural characteristic was maintained after

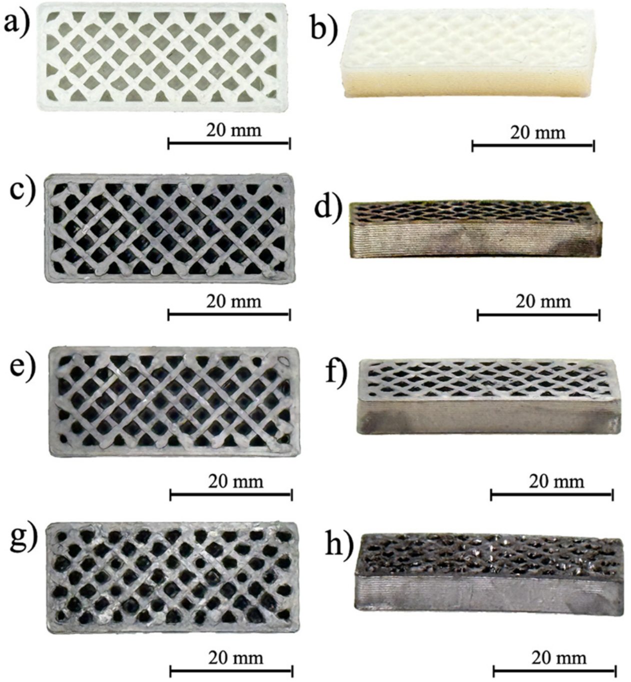

Fig. 2 Front and side views of 3D-printed PLA samples after (a and b) 0 (cycle 0), (c and d) 3 (cycle 3), (e and f) 6 (cycle 6), and (g and h) 9 (cycle 9) dip-coating cycles.

coating and is intrinsic to the printing design rather than the coating process.

Characterization methods

Thermogravimetric analysis (TGA). Thermal stability of the GNP-coated 3D-printed PLA samples (cycles 0, 3, 6, and 9) was evaluated using a thermogravimetric analyzer (Q500, TA Instruments, New Castle, USA). Approximately 3–10 mg (typically ~5 mg) of each sample was heated from 25 °C to 500 °C at a constant rate of 10 °C min^{-1} under a nitrogen atmosphere with a flow rate of 20 mL min^{-1}.

Contact angle measurement. Surface wettability of untreated, etched, and GNP-coated PLA samples was assessed using a drop shape analyzer (DSA25, KRÜSS Scientific Instruments, North Carolina, USA). A droplet of GNP ink was dispensed *via* a 20G needle onto the non-porous side (capped-side) of each sample, and the contact angle was recorded over 4 seconds at 30 fps, using the Young–Laplace fitting method for accuracy. Contact angle measurements were performed on at least $n \geq 5$ independent locations per sample, and the reported values represent the mean ± standard deviation.

Morphological and elemental analysis. Surface and cross-sectional morphology of GNP-coated samples were examined using a Field Emission Scanning Electron Microscope (FE-SEM; Quanta FEG 250, FEI Company, Hillsboro, USA), operated in both secondary and backscattered electron modes. All specimens were sputter-coated with a thin platinum layer to minimize charging effects.

Surface morphology was imaged directly on intact coated samples, while cross-sectional analysis was performed on cryo-fractured samples prepared using a Leica Ultracut UTC ultramicrotome (Wetzlar, Germany) at −80 °C. Coating thickness and delaminated regions (before and after tape peeling) were analyzed using ImageJ software. Additionally, ash residues from combusted samples were embedded in epoxy (Sigma-Aldrich, St Louis, USA) and mounted on SEM stubs for post-combustion imaging.

Elemental composition was assessed *via* Energy-Dispersive X-ray Spectroscopy (EDS), using a Quantax system (Bruker Nano GmbH, Berlin, Germany) equipped with an XFlash 5030 SDD detector and Bruker SVE III pulse processor.

Tape peeling test. Adhesion strength of the GNP coatings on 3D-printed PLA samples was evaluated using a modified tape peeling method that combined both qualitative and quantitative analysis. The baseline method followed ASTM D3359,[63] Method B (cross-hatch test), typically used as a qualitative benchmark for coatings below 150 μm thickness.

A carpet-cutting blade was used to generate two sets of five parallel cuts, each 20 mm long, 2 mm apart, arranged perpendicularly to form a cross-hatch grid (see Fig. 3c).

To improve reproducibility and gain quantitative insight, this test was integrated with a universal tensile testing machine (Instron 5965, Norwood, USA), converting the procedure into a force-measured delamination test.

This approach allowed the measurement of the maximum force required to initiate and propagate coating delamination, thereby providing a quantitative metric for coating durability. Two cross-hatch grids were prepared per sample—one for surface imaging and one for cross-sectional analysis post-delamination.

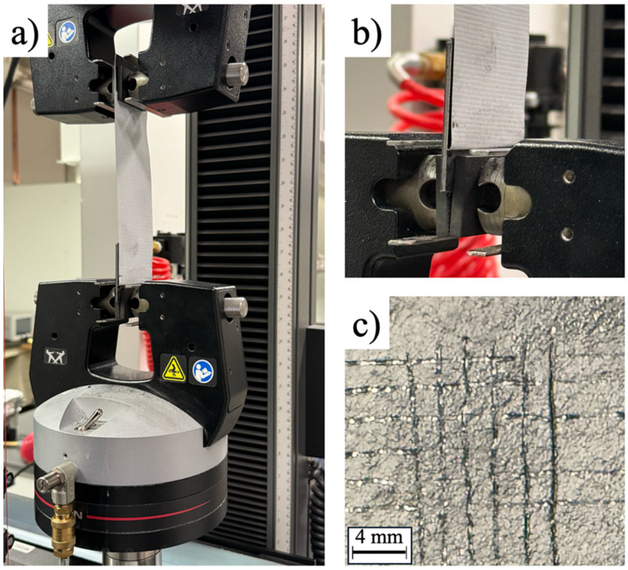

Fig. 3 Images of (a) and (b) set-up for 180° tape peeling testing, and (c) ASTM D3359 method B cross-hatch cut grid.

Testing was conducted at 23 °C. A 3M™ DT8 duct tape (Saint Paul, USA) strip was applied to the coated surface and preloaded with 400 N. The tape was then folded back 180°, attached to the upper grip, and peeled off in tensile mode at 3000 mm min^{-1}, while the sample was clamped from below (15 mm gauge length), as shown in Fig. 3a and b. Each test was repeated three times per sample to ensure reproducibility.

Electrical conductivity measurement. Surface electrical conductivity of the GNP-coated 3D-printed PLA samples was measured using a Loresta GP resistivity meter (MCP-T610, Mitsubishi Chemical Co., Japan) equipped with a four-point probe head (MCP-TP08P, Mitsubishi Chemical Co., Japan). This setup enabled accurate surface resistance measurements while minimizing contact resistance effects.

Electromagnetic interference (EMI) shielding effectiveness. EMI shielding effectiveness (SE) of the coated porous 3D-printed samples was evaluated using an Agilent E5071C vector network analyzer (ENA Series, 300 kHz–20 GHz), in conjunction with a WR-90 rectangular waveguide operating in the X-band frequency range (8.2–12.4 GHz). Shielding effectiveness was calculated based on the scattering parameters (*S*-parameters), using the logarithmic ratio of transmitted to incident power, expressed in decibels (dB).[64]

EMI shielding calculations. The electromagnetic shielding properties were evaluated using a vector network analyzer (VNA) in the X-band frequency range.[65] The scattering parameters (*S*-parameters) were recorded in the form of a 2 × 2 matrix (eqn (1)):

$$S = \begin{bmatrix} S_{11} & S_{12} \\ S_{21} & S_{22} \end{bmatrix} \quad (1)$$

where S_{11} and S_{22} represent reflection coefficients, and S_{21} and S_{12} represent transmission coefficients. The reflectance (R) (eqn (2)) and transmittance (T) (eqn (3)) were calculated from the squared magnitudes of the measured parameters:

$$R = |S_{11}|^2 \tag{2}$$

$$T = |S_{21}|^2 \tag{3}$$

The absorbance (A) was determined using eqn (4):

$$A = 1 - (R + T) \tag{4}$$

The reflection ($\mathrm{SE_R}$) (eqn (5)) and absorption ($\mathrm{SE_A}$) shielding (eqn (6)) components were calculated as:

$$\mathrm{SE_R}(\mathrm{dB}) = -10\log(1 - R) \tag{5}$$

$$\mathrm{SE_A}(\mathrm{dB}) = -10\log\left(\frac{T}{1 - R}\right) \tag{6}$$

The total shielding effectiveness ($\mathrm{SE_T}$) was obtained from eqn (7):

$$\mathrm{SE_T}(\mathrm{dB}) = \mathrm{SE_R} + \mathrm{SE_A} \tag{7}$$

Limiting oxygen index (LOI) testing. Flame retardancy was assessed *via* Limiting Oxygen Index (LOI) testing, following the ASTM D2863 standard. Tests were conducted using a commercial LOI apparatus (AT-P6012A, Amade Technology Co., Ltd, Hong Kong, China). This method determines the minimum oxygen concentration required in an oxygen–nitrogen mixture to sustain sample combustion for at least 3 minutes under ambient conditions. LOI measurements were conducted on $n \geq 3$ specimens per condition, and results are reported as mean ± standard deviation.

Results and discussion

Thermal properties

The thermal behavior of the GNP-coated 3D-printed PLA samples (cycles 0, 3, 6, and 9) was analyzed using thermogravimetric analysis (TGA) and derivative thermogravimetric (DTGA) curves, as shown in Fig. 4. The corresponding thermal parameters are summarized in Table 1.

Table 1 Thermogravimetric data of 3D-printed PLA samples with increasing GNP coating cycles

	Property			
Sample name	ODT (°C)	$T_{\text{d-max}}$ (°C)	Char content (%)	GNP content (%)
Cycle 0	311.7 ± 0.5	353.6 ± 0.6	1.6 ± 0.2	—
Cycle 3	312.1 ± 0.4	359.4 ± 0.5	4.2 ± 0.3	2.6 ± 0.1
Cycle 6	325.1 ± 0.6	368.2 ± 0.5	5.4 ± 0.2	3.8 ± 0.1
Cycle 9	339.2 ± 0.8	378.1 ± 0.5	7.1 ± 0.3	5.5 ± 0.2

Cycle number indicates the number of dip-coating repetitions with GNP. Note: the effective GNP content for each coating cycle was estimated from the increase in residual char yield relative to the uncoated PLA scaffold (Cycle 0), assuming that the additional thermally stable residue originates primarily from the carbonaceous GNP coating. Values are reported as mean ± standard deviation from replicate TGA measurements.

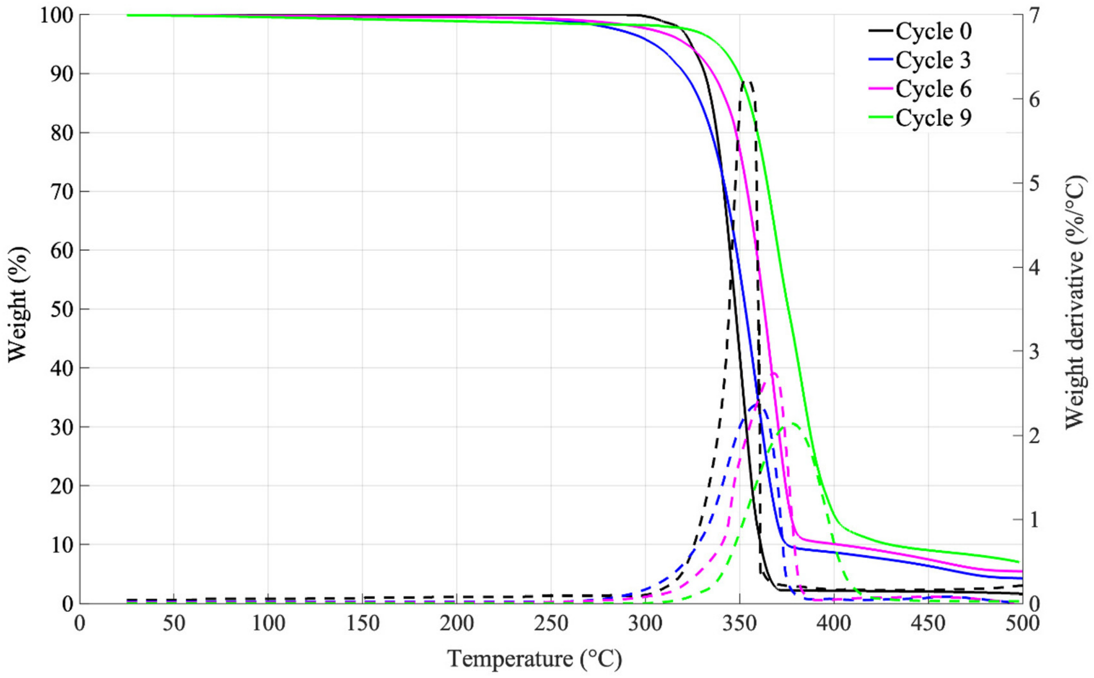

Fig. 4 Thermogravimetric (TGA, solid lines) and derivative thermogravimetric (DTG, dashed lines) curves of PLA scaffolds coated with 0, 3, 6, and 9 GNP dip-coating cycles.

The uncoated (neat) PLA sample, referred to as "cycle 0", exhibited a sharp mass loss over a narrow temperature range, with an Onset Degradation Temperature (ODT) of 311.7 °C and a Maximum Degradation Temperature ($T_{\text{d-max}}$) of 353.6 °C. These values are typical of pristine PLA and indicate its limited thermal stability.[66]

Progressive dip-coating with GNP led to two major improvements:

(1) a consistent increase in both ODT and $T_{\text{d-max}}$, and

(2) a noticeable broadening of the DTGA peaks.

The $T_{\text{d-max}}$ increased by 5.7 °C (cycle 3), 14.5 °C (cycle 6), and 24.4 °C (cycle 9) compared to neat PLA, demonstrating the thermal shielding effect of the GNP coating.[67,68]

The broadening of the DTGA peaks suggests a reduction in the mass loss rate (MLR), indicating that the thermal degradation of the polymer became more gradual with increasing GNP coverage. This is attributed to the barrier properties of GNP, which hinder heat and gas transfer, delaying the onset and peak of thermal decomposition.

Char residue, a key indicator of flame retardancy, also increased significantly with coating thickness. While neat PLA yielded only 1.6% residual char, samples with 3, 6, and 9 GNP coating cycles produced 4.3%, 5.4%, and 7.1% char, respectively.

These enhancements: higher $T_{\text{d-max}}$, reduced MLR, and increased char yield—collectively indicate that the GNP layer acts as a thermally protective barrier, effectively improving the fire resistance of the PLA scaffold. This effect likely arises from the GNP film's ability to delay volatile release and promote the formation of a dense char layer, thus elevating the overall thermal degradation threshold.[68–70]

Furthermore, the difference in char yield between the neat and coated samples offers a practical estimation of GNP uptake during the dip-coating process.

The effective GNP content was estimated from the TGA residual mass fraction (char yield) by comparing coated samples with the uncoated PLA scaffold (Cycle 0). Assuming that the increase in final residue primarily originates from the thermally stable carbonaceous fraction introduced by the GNP coating, the GNP loading for a sample coated with n cycles was calculated as:

$$W_{\mathrm{GNP},n}\ (\%) = Y_{\mathrm{char},n}\ (\%) - Y_{\mathrm{char},0}\ (\%),$$

where $Y_{\mathrm{char},n}$ is the residual mass fraction of the n-cycle coated sample and $Y_{\mathrm{char},0}$ is the residual mass fraction of the uncoated PLA scaffold. For example, $Y_{\mathrm{char},0} = 1.6 \pm 0.2\%$ and $Y_{\mathrm{char},3} = 4.2 \pm 0.3\%$, yielding $W_{\mathrm{GNP},3} = 2.6\%$. Based on this calculation, the GNP loading for cycles 3, 6, and 9 was estimated to be approximately 2.6 wt%, 3.8 wt%, and 5.5 wt%, respectively.

This calculation provides an estimate of GNP loading derived from residue differences and may include minor contributions from coating additives (*e.g.*, PVP) or potential variations in PLA charring behavior.

Surface wettability, contact angle behavior, and interfacial capillarity

Fig. 5 summarizes the static and dynamic contact angle behavior of untreated PLA, NaOH-etched PLA, and PEI-modified PLA, demonstrating how sequential surface modifications shape the wetting and interfacial properties critical for successful dip coating.

The untreated PLA sample shows a moderate initial contact angle of 39.8°, while NaOH-etched PLA exhibits a slightly higher angle of 44.7°, despite increased surface roughness. While the Wenzel model predicts that roughness should enhance wettability by amplifying the inherent surface energy, the observed increase in contact angle instead aligns with the Cassie–Baxter regime, where micro-roughness entraps air beneath the droplet, decreasing effective liquid–solid contact.[71–73] This behavior illustrates that roughness alone does not guarantee improved wettability, particularly when hierarchical pores and etched microcavities are present on 3D-printed PLA surfaces.

Upon subsequent modification with polyethyleneimine (PEI), the initial contact angle remains nearly unchanged (44.6°); however, a sharp drop to 12.2° within 4 seconds is observed, signaling a dramatic improvement in dynamic wettability. This rapid wetting behavior is indicative of enhanced surface polarity, driven by the introduction of hydrophilic amine (–NH_2) functional groups from PEI.[62] These groups increase the polar component of the surface free energy, promoting stronger interactions with both water and polar ink dispersions such as the GNP-based coating used in this study.

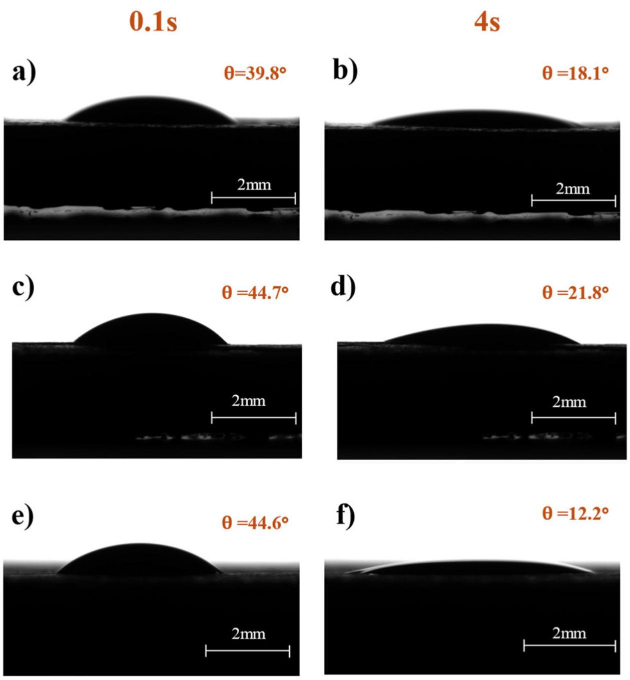

Fig. 5 Contact angle measurements at 0.1 s and 4 s for (a and b) untreated PLA, (c and d) NaOH-etched PLA, and (e and f) PEI-modified PLA.

Although the initial static contact angle does not immediately reflect this chemical shift, the dynamic response highlights an activated and highly wettable surface, suitable for reliable ink anchoring and rapid spreading during dip coating.[74–76]

The combined effect of NaOH etching and PEI modification creates a well-defined interfacial environment that promotes robust GNP coating adhesion. NaOH etching increases nanoscale roughness and available surface area, providing mechanical interlocking sites that help anchor deposited nanocarbon layers. PEI, on the other hand, introduces a dense layer of polar and hydrogen-bonding functional groups, which improves chemical compatibility, suppresses dewetting, and enhances electrostatic interactions with GNP platelets.[57,58] This dual modification strategy mitigates the hydrophobic behavior associated with surface roughening and results in a more wettable surface, which is consistent with enhanced interfacial interactions and improved coating affinity.[59]

These wetting transitions directly influence the dip-coating process. Under the selected withdrawal conditions, the coating behavior corresponds to the Landau–Levich–Derjaguin (LLD) regime, where film formation is governed by a balance between viscous drag and surface tension forces.[77–79] Maintaining a low capillary number ensures that the deposited ink forms thin, continuous, and uniform sub-micron films ideal for establishing surface-percolated conductive networks after drying. Additionally, the architected lattice of the 3D-printed PLA—composed of struts, pores, and interconnected junctions—acts analogously to a microfiber scaffold, providing geometric anchoring sites that minimize runoff, promote capillary pinning, and stabilize the coating across complex topographies.[80,81] Together, the enhanced wettability, increased surface polarity, and favourable capillary dynamics enable controlled GNP deposition, ultimately yielding uniform, adherent coatings essential for high-performance multifunctional structures.

To quantitatively assess surface wettability, the average water contact angle measured at 4 s for each surface treatment is presented with corresponding standard deviations in Fig. 6.

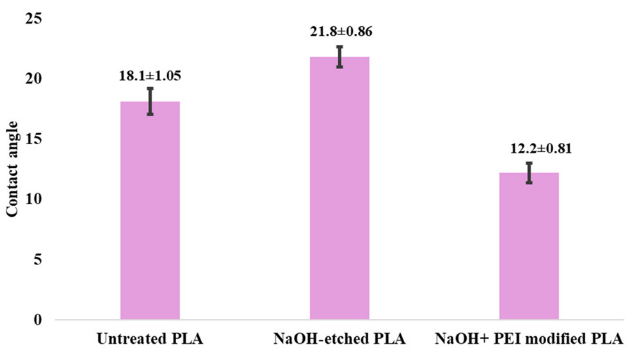

Fig. 6 Average water contact angle of untreated PLA, NaOH-etched PLA, and NaOH + PEI modified PLA measured at 4 s after droplet deposition. Values represent mean ± standard deviation (n = 5).

Surface morphology

To further elucidate the effect of surface pretreatment, FESEM micrographs of the untreated PLA scaffold, NaOH-etched PLA, and NaOH + PEI-modified PLA were examined (Fig. 7). The untreated PLA exhibits a relatively smooth surface, whereas NaOH treatment induces homogeneous surface roughening and micron-scale texturing. Such morphological changes are expected to enhance mechanical interlocking with the subsequent GNP coating.

Following PEI modification, the etched morphology remains visible, while the surface appears more uniformly covered and smoothened. This observation is consistent with the presence of an interfacial modifying layer that may contribute to improved coating adhesion. In the cross-sectional FESEM images, a thin interfacial region consistent with the PEI-treated surface can be distinguished (Fig. 8).

Coating morphology

Fig. 9 presents the surface morphology of GNP-coated 3D-printed porous PLA structures across different dip-coating cycles. The first, second, and third rows correspond to samples coated for 3, 6, and 9 cycles, respectively. In Fig. 9a, e and i, the diamond-like porous lattice geometry remains visible across all conditions, indicating that the macro-architecture of the 3D-print is preserved throughout the coating process. However, as the number of coating cycles increases, the pore openings become progressively narrower. By the 9th cycle, partial pore blockage is observed, reflecting a substantial increase in overall coating thickness and deposition density.

High-magnification images (Fig. 9c, g and k) focus on individual printed struts and reveal the microstructural arrangement of the deposited GNPs. The FESEM images suggest a laminar or platelet-stacked morphology characteristic of graphene nanoplatelet assemblies. As PVP was employed as a dispersing agent during ink preparation, a thin residual polymer phase may remain at platelet interfaces following solvent evaporation; however, this interphase was not directly resolved in the present study. Importantly, this surface-connected architecture differs from the conductive pathways seen in traditional nanocomposites governed by classical bulk percolation theory. In polymer composites, nanoparticle dispersion and network formation are constrained by the semi-solid polymer matrix. In contrast, dip-coated thin films lack this constraint, allowing for enhanced lateral connectivity and even partial nanoparticle agglomeration, particularly in the uppermost coating layers.[82–84]

After up to six coating cycles, the morphology becomes more compact and homogeneous. The inter-platelet air gaps shrink considerably, and the graphene layers form a denser stack along the PLA surface. However, after nine coating cycles, the topmost layers appear increasingly flaky and less consolidated, with more irregular platelet spacing. This morphological shift may indicate the onset of a saturation-like behavior in the coating process. In early cycles, smaller GNPs effectively fill voids and consolidate the underlying structure.

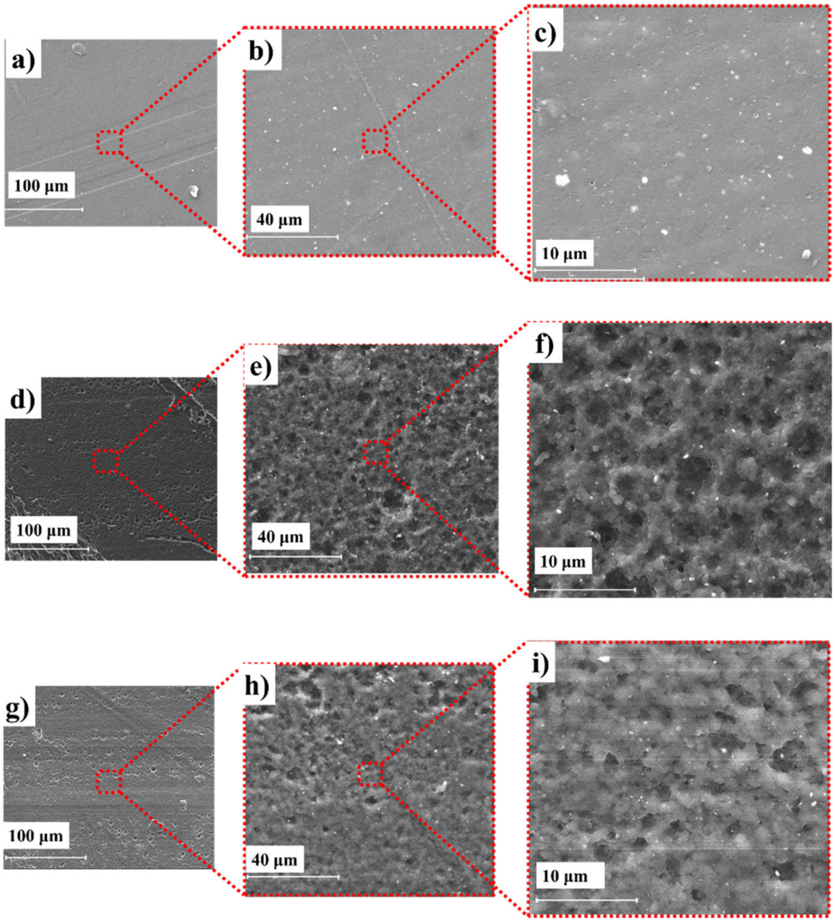

Fig. 7 FESEM micrographs (secondary electron mode) of untreated PLA (a–c); (d–f) NaOH-etched PLA; (g–i) NaOH + PEI-modified PLA.

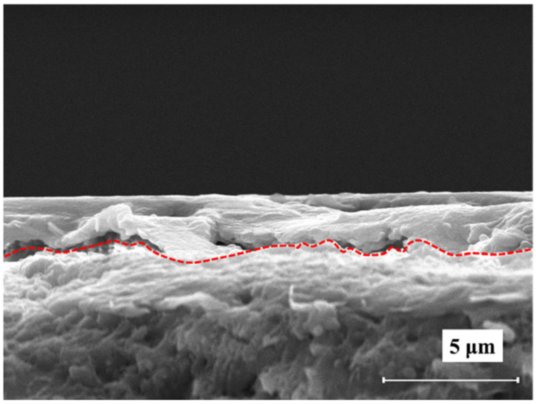

Fig. 8 Cross-sectional FESEM micrograph (secondary electron mode) of the NaOH-etched and PEI-modified PLA scaffold. The dashed line indicates the approximate boundary between the near-surface treated region and the PLA bulk.

Beyond a certain point—evident in the 9-cycle sample—further deposition adds loosely stacked material, increasing surface roughness and potentially limiting further film densification.[72,85]

Although these higher-cycle samples appear rougher and exhibit localized agglomeration, this does not necessarily imply greater variation in coating thickness. Instead, it reflects a shift in the mode of film growth—from consolidation-dominated to surface accumulation. This transition emphasizes the importance of balancing coating thickness with film integrity, as excessive deposition may hinder adhesion, create mechanical weak points, or introduce electrical inconsistencies in functional coatings. The data suggest that six coating cycles may represent an optimal balance between film thickness, connectivity, and uniformity.

Cross-sectional characterization of GNP-coated layers

To evaluate coating uniformity, thickness, and structural integrity, cross-sectional FESEM analysis was performed on GNP-coated 3D-printed PLA samples after 3, 6, and 9 dip-coating cycles. Fig. 10 presents representative cross-sectional images for each coating condition. These images provide additional insight into how coating cycles influence not only layer thickness but also morphological alignment within the coating.

As summarized in the inset table in Fig. 10, the average GNP layer thickness increased substantially with additional coating cycles. For the 3-cycle sample, the layer measured

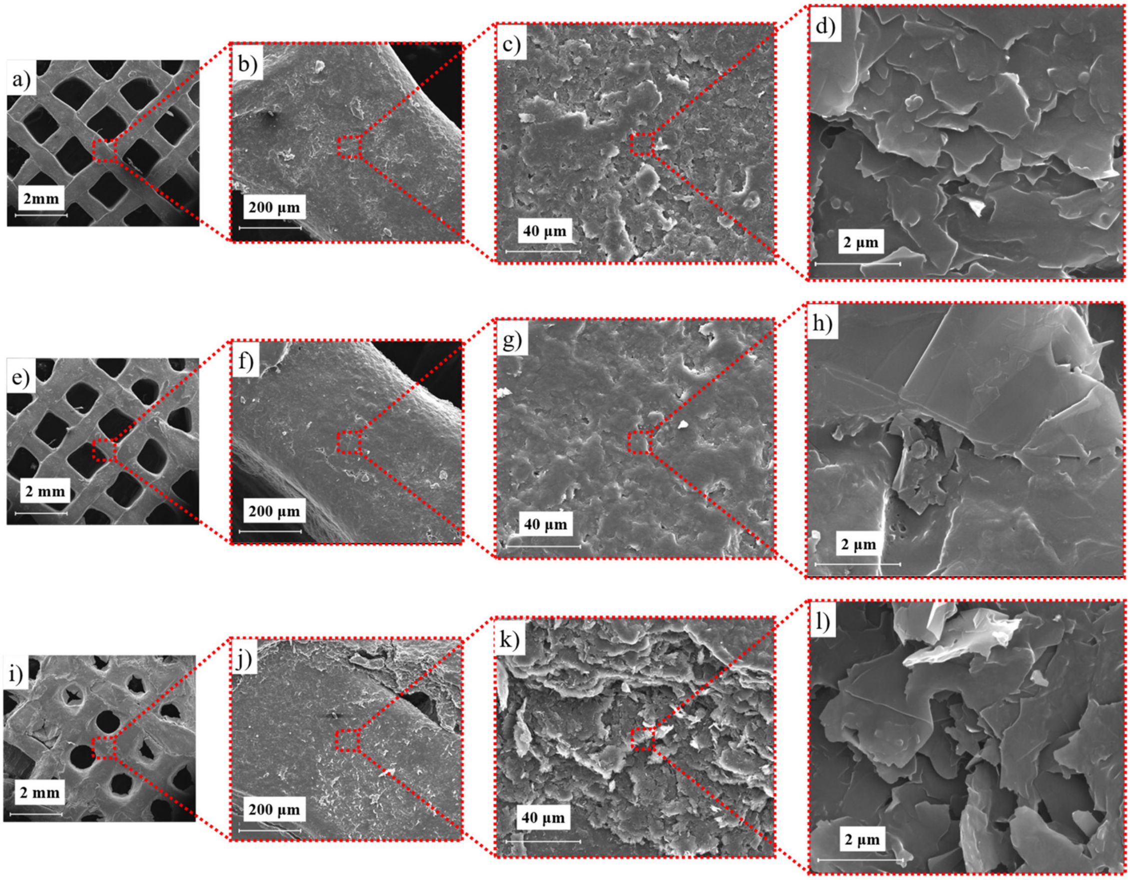

Fig. 9 FESEM micrographs (secondary electron mode) of the surface of 3D-printed PLA samples at various magnifications: (a–d) 3 coating cycles, (e–h) 6 coating cycles, and (i–l) 9 coating cycles.

18.85 µm in thickness. This value increased by approximately 253.6% and 418.6% for the 6-cycle and 9-cycle samples, respectively, approaching 100 µm after nine cycles. The steady and predictable increase in layer thickness suggests good repeatability and scalability of the dip-coating process.

A comparative examination of the high-magnification cross-sections (Fig. 10c and e) reveals another important trend: the layered GNP structures become more uniform and stratified with increasing coating cycles. In both the 6-cycle and 9-cycle samples, the GNP sheets exhibit a horizontally aligned, laminated morphology oriented nearly parallel to the PLA substrate surface.

Panels (a), (b), and (d) show the interface between the PLA substrate and the GNP coating layer, with arrows identifying the respective regions and the dashed line indicating the coating–substrate boundary. Panels (c) and (e) provide higher-magnification views of the GNP coating layer only, where the PLA substrate is not visible.

This in-plane alignment of the graphene nanoplatelets is critical, as it introduces several functional advantages. First, the horizontal stratification increases diffusion path tortuosity, which enhances barrier properties by impeding the penetration of gases or liquids through the coating. Second, the ordered stacking contributes to improved coating compactness, minimizing interstitial voids and enhancing mechanical integrity. Third, and most notably, the parallel arrangement of conductive graphene layers facilitates multiple internal reflections of incident electromagnetic (EM) waves, thereby enhancing overall EMI shielding performance.[75,76,86–89]

This microstructural arrangement—achieved through a scalable dip-coating process—illustrates the successful integration of both architectural control and material alignment, enabling multifunctional coatings that are mechanically robust, electrically conductive, and suitable for advanced EMI shielding applications.

Peeling resistance

The adhesion strength and mechanical durability of the GNP coatings on 3D-printed PLA substrates were evaluated using a tape peeling test. This method provides both quantitative and qualitative assessment of coating adhesion by examining cross-sectional thickness changes *via* FESEM and measuring the force required to initiate delamination.

Fig. 11 presents the cross-sectional FESEM images of GNP-coated samples before (left column) and after (right column) tape peeling for 3, 6, and 9 coating cycles. For the 3-cycle

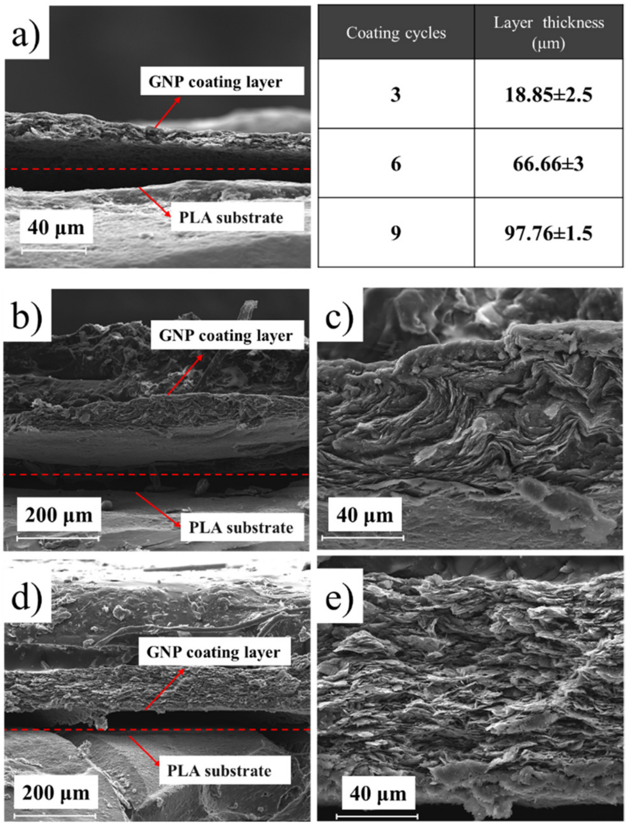

Coating cycles	Layer thickness (µm)
3	18.85±2.5
6	66.66±3
9	97.76±1.5

Fig. 10 Cross-sectional FESEM images (secondary electron mode) of 3D-printed PLA samples dip-coated with GNP for (a) 3 cycles, (b and c) 6 cycles, and (d and e) 9 cycles, shown at increasing magnifications.

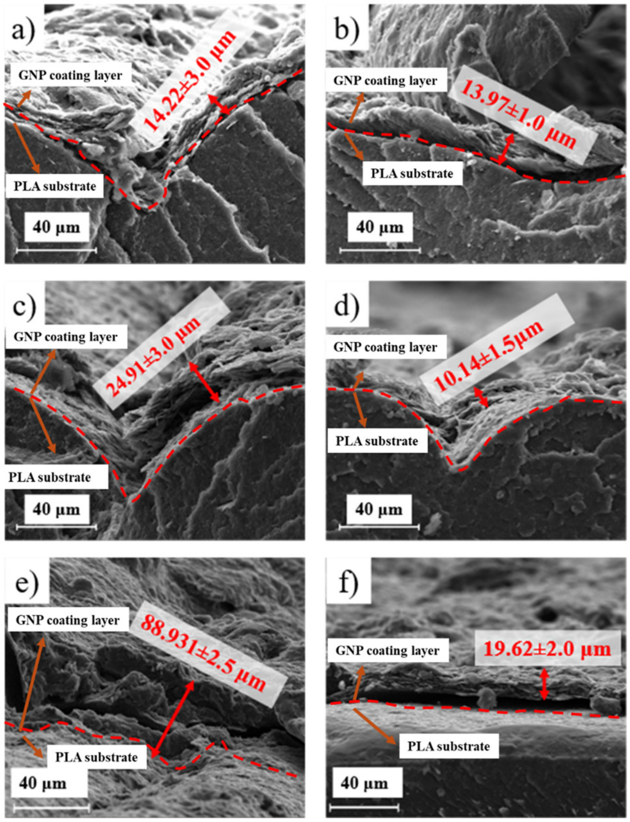

Fig. 11 Cross-sectional FESEM images (secondary electron mode) of GNP-coated 3D-printed PLA samples before (left column) and after (right column) tape peeling: (a and b) 3-cycle sample; (c and d) 6-cycle sample; (e and f) 9-cycle sample.

sample (Fig. 11a and b), the initial GNP thickness was 14.2 µm, and approximately 1.7% of the coating was removed after three peeling cycles. The minimum delamination force measured for this sample was 0.75 MPa, indicating strong coating adhesion at lower thickness.

In contrast, samples coated for 6 and 9 cycles exhibited substantially greater coating loss. For the 6-cycle sample (Fig. 11c and d), approximately 59.3% of the original 24.9 µm layer was removed, while the 9-cycle sample (Fig. 11e and f) showed 77.9% removal from an initial thickness of 88.9 µm. The corresponding delamination forces decreased to 0.65 MPa (6 cycles) and 0.55 MPa (9 cycles). These results indicate a progressive reduction in peel resistance with increasing coating thickness.

This trend is consistent with a transition in failure mode. While thinner coatings appear to fail primarily at or near the coating–substrate interface, thicker multilayer coatings show increased susceptibility to separation within the GNP layers. As coating thickness increases, the GNP–GNP interfaces—especially in the uppermost layers—become more susceptible to delamination, likely due to reduced compaction and weaker van der Waals forces between platelets.[90]

The improved adhesion observed in the 3-cycle coating is consistent with the combined NaOH and PEI surface pretreatment, which enhances surface roughness and modifies the interfacial region.[91]

Even in thicker coatings, a residual GNP layer (10–20 µm) remained after peeling, indicating that the base coating layer maintains partial adhesion to the PLA substrate.

These results underscore the importance of balancing coating thickness with cohesive strength, especially for mechanically loaded applications.

The dashed red line indicates the coating–substrate interface. Arrows identify the GNP coating layer and PLA substrate. Measured coating thickness values are reported as mean ± standard deviation from multiple measurements.

Cross-hatch adhesion grading and surface delamination behavior

Fig. 12 shows the post-peeling surface morphology of cross-hatch grids applied to GNP-coated 3D-printed PLA samples after 3, 6, and 9 dip-coating cycles.[92,93] This visual assessment, based on the ASTM D3359 Method B standard, complements the quantitative peeling tests and provides insight into the extent and distribution of delamination across the coated surfaces.

In the 3-cycle sample (Fig. 12a and b), no visually detectable delamination was observed within the grid squares or along their edges. The coating remained fully intact after tape

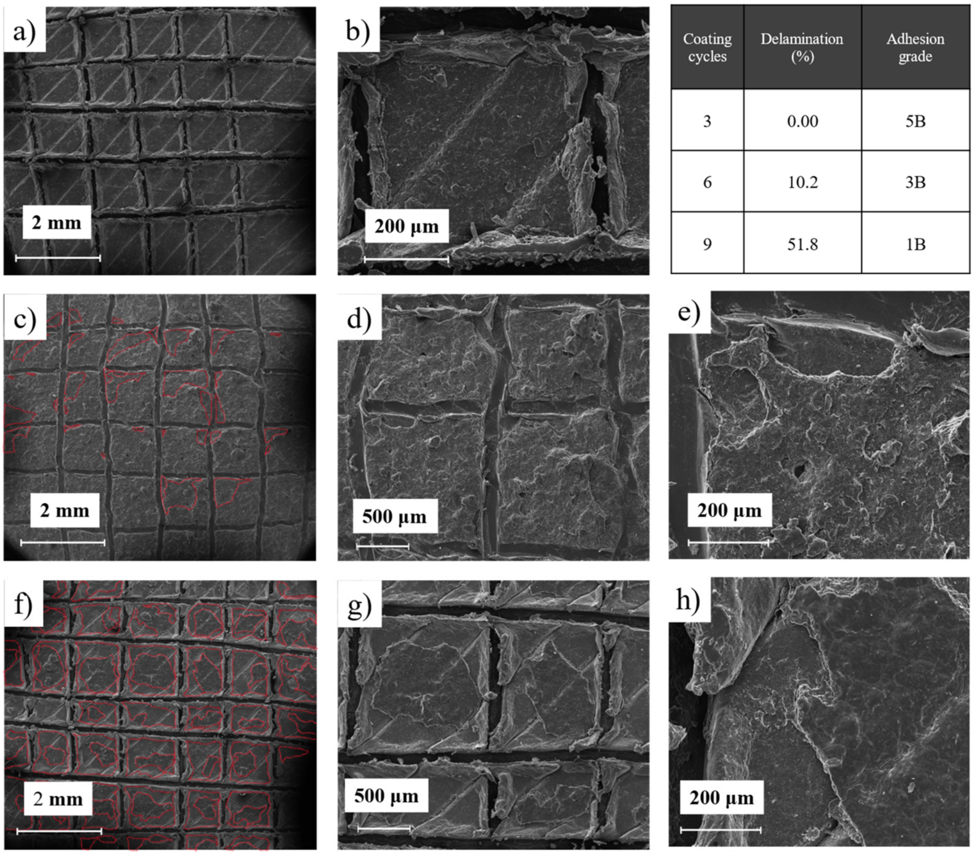

Coating cycles	Delamination (%)	Adhesion grade
3	0.00	5B
6	10.2	3B
9	51.8	1B

Fig. 12 Post-peeling surface morphology of cross-hatch cut grids (secondary electron mode) for GNP-coated 3D-printed PLA samples: (a and b) 3 cycles (5B rating); (c–e) 6 cycles (3B rating); (f and g) 9 cycles (1B rating). Red-marked regions indicate visible delamination.

removal, qualifying for the highest adhesion rating of 5B. This strong adhesion performance is consistent with strong interfacial adhesion and film cohesion, consistent with earlier mechanical tests indicating high peel strength and minimal thickness loss.

At 6 coating cycles, partial delamination becomes evident. In Fig. 12c, regions marked in red highlight delaminated zones, which account for approximately 10% of the total grid area. According to the ASTM grading scale, this corresponds to a moderate adhesion rating of 3B. As shown in Fig. 12d and e, delamination is primarily localized at the corners of the squares, while central regions largely retain their coating. This pattern may be associated with stress concentration effects and slightly lower compaction in outer layers may initiate failure under peeling.

In the 9-cycle sample (Fig. 12f and g), the delamination is significantly more widespread, occurring in nearly all square corners and extending toward the center in several regions. The total delaminated area is estimated at ~52%, yielding a lower adhesion rating of 1B. Despite the apparent degradation, it is important to note that the entire GNP layer is not necessarily removed. In many areas, only the uppermost GNP layers are lifted during peeling, while residual base layers remain adhered to the PLA substrate. However, per standard evaluation criteria, any visually lifted or fractured coating—regardless of partial retention—is classified as delaminated and factored into the adhesion grade.

These results underscore the impact of coating thickness on peel behavior. Thinner coatings (3 cycles) exhibit high interfacial strength and cohesive integrity, while thicker, multilayer coatings become more susceptible to surface cracking and edge delamination under stress. The visual grading trends are consistent with measured peel forces and cross-sectional damage analysis, confirming that optimal coating design must balance functional thickness with mechanical robustness.

To validate the proposed adhesion mechanism, post-peel FESEM analyses were conducted for untreated PLA, NaOH-etched PLA, and PEI-modified PLA after identical coating conditions (3 cycles). As shown in Fig. S1, untreated PLA displayed the weakest coating adhesion, whereas NaOH or PEI alone yielded partial improvement; the combined NaOH + PEI treatment showed the strongest coating adhesion, consistent with contributions from both mechanical interlocking and interfacial interactions.

Electrical conductivity

Fig. 13 presents the surface electrical conductivity of architected, 3D-printed PLA samples coated with graphene nanoplatelets

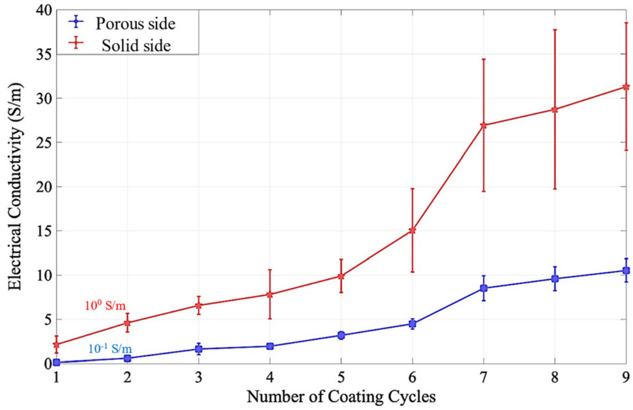

Fig. 13 Electrical conductivity *versus* number of coating cycles for solid and porous side of the coated 3D-printed PLA samples.

(GNP) *via* dip-coating for 1 to 9 cycles, measured separately on the porous (lattice-exposed) and solid (capped) sides. As expected, the conductivity of neat PLA was negligible (~10^{-13} S m^{-1}), confirming its insulating nature. However, even after just one or two coating cycles, a substantial increase in conductivity was observed: the porous side reached ~10^{-1} S m^{-1}, while the solid side exceeded 1 S m^{-1}. These early improvements reflect the rapid establishment of interconnected conductive pathways across the surface, well before any bulk saturation, highlighting the role of surface percolation in driving electrical performance.[94–96] Conductivity continued to increase steadily with additional coating cycles, displaying a near-linear trend rather than the abrupt jump typically associated with classical percolation theory. This deviation reinforces the idea that conductivity arises not from volumetric filler thresholds but from the progressive densification and continuity of the GNP film across the architected PLA substrate.[96] A notable uptick in conductivity was observed around cycle 6, potentially marking the onset of a more uniformly connected surface network.

Across all samples, the solid side consistently demonstrated higher conductivity than the porous side, attributable to the smoother surface and absence of surface voids that can disrupt film continuity. However, as the number of coating cycles increased, the conductivity gap between the two sides diminished, with the solid-to-porous conductivity ratio dropping from 16.4 to 2.9. This convergence suggests that GNP ink deposition became increasingly uniform, with more complete infiltration and coverage of the lattice struts and pore walls.

The structural topology of the 3D-printed lattice plays a key role in this behavior. On the porous side, GNP deposition follows the contours of the interconnected struts, forming filamentous networks rather than flat films. This architecture supports the directional propagation of conductive pathways, resulting in mild electrical anisotropy that is gradually suppressed by repeated coating cycles. Ultimately, the architecture-enabled surface percolation mechanism allows the conductive network to span the full geometry of the porous scaffold with minimal material input.

Importantly, this dip-coating strategy achieved comparable or superior electrical performance (10^{-1} to 10^{0} S m^{-1}) relative to prior studies that required significantly higher filler loadings. Lee *et al.*[97] achieved ~10^{0} S m^{-1} using CNT on cellulose paper with 10 times of coatings; Souri *et al.*[98] reported 10^{-2} to 10^{-1} S m^{-1} for GNP-coated yarns; Tian *et al.*[99] obtained 6.43 S m^{-1} with 60 wt% graphene on nylon. In contrast, composite approaches require >10 wt% GNP to reach 10^{0} S m^{-1}.[100–104] In contrast, the present work attained these results using <2.62 wt% GNP, demonstrating material efficiency, process scalability, and excellent compatibility with complex 3D-printed geometries.

EMI shielding

Fig. 14 presents the total shielding effectiveness (SE_T) of architected, 3D-printed PLA structures as a function of GNP dip-coating cycles. A nearly linear trend is observed, where SE_T increases steadily from ~0 dB (uncoated) to ~25 dB after nine cycles. Importantly, no sharp threshold or saturation behavior emerges within the studied range, suggesting a controlled, cycle-dependent enhancement in shielding performance.

After only two dip-coating cycles, the structure achieves a SE_T of ~10 dB—equivalent to 90% attenuation of incident electromagnetic waves. With six coating cycles, the SE_T exceeds 20 dB, a widely accepted benchmark for commercial EMI shielding applications. By the ninth cycle, shielding effectiveness approaches 25 dB, corresponding to ~99.7% attenuation. This performance is notable considering the minimal filler content and the lightweight, porous nature of the substrate.

The observed linearity closely mirrors the progressive increase in GNP layer thickness and conductivity across cycles. Given the superior electromagnetic properties of GNP relative to PLA, it is clear that the GNP coating becomes the dominant shielding medium, with its growth directly translating into improved SE_T.[60,105]

To elaborate on the underlying EMI shielding mechanism of the GNP-coated 3D-printed porous PLA structure, the key

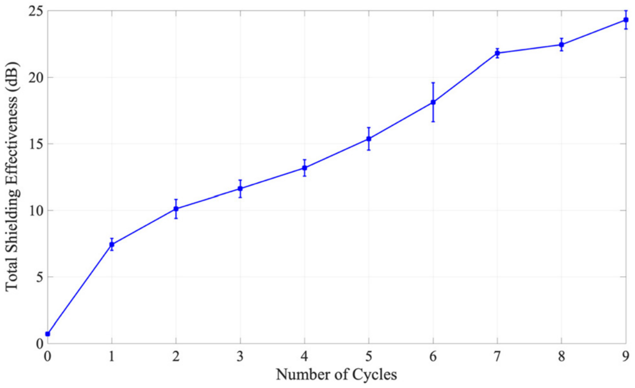

Fig. 14 Total shielding effectiveness (SE_T) of 3D-printed porous PLA samples as a function of graphene nanoplatelet (GNP) dip-coating cycles.

factors affecting both EM wave reflection and absorption are as follows:

- Reflection: As a conductive material, GNP serves as the outer coating on the PLA substrate and acts as the initial interface for incident EM waves. Due to impedance mismatch, a portion of the wave is reflected. Reflection is further enhanced through ohmic loss (Joule heating) induced by the GNP's electrical resistivity.[106] As shown in Fig. 13, the electrical conductivity of the GNP layer increases linearly with coating cycles, leading to greater reflection due to increased impedance mismatch.[105] Additionally, the skin effect contributes to reflection by limiting wave penetration in more conductive materials and/or at higher frequencies, thereby reducing absorption.[26,107]
- Absorption: EM wave absorption occurs through several mechanisms. Ohmic loss dissipates wave energy *via* electrical resistance in the GNP layer.[108] Dipole polarization-induced loss also plays a role, where GNP dipoles align and reorient within oscillating EM fields, generating heat due to internal friction.[27] Furthermore, the heterogeneous structure introduces interfacial polarization, described by the Maxwell–Wagner–Sillars (MWS) effect. This occurs at the GNP–PLA interface, where differing conductivities result in charge accumulation and rearrangement.[26,109] A larger interfacial area and a more conductive, thicker GNP layer facilitate greater charge separation, thus enhancing energy loss and enabling lightweight, efficient EMI shielding.[110,111]

Fig. 15 illustrates the total shielding effectiveness (SE_T) of 3D-printed porous PLA structures dip-coated with graphene nanoplatelets (GNP) across the X-band frequency range (8.2–12.4 GHz) for four coating levels: 3, 6, and 9 cycles. The uncoated porous PLA structure (cycle 0) provides negligible shielding, while the SE_T increases steadily with additional coating cycles. A distinct resonance peak near 10 GHz appears for all samples, with its amplitude growing consistently as coating thickness increases. This trend reflects the stronger interaction between EM waves and the progressively developed conductive GNP network.[112–114]

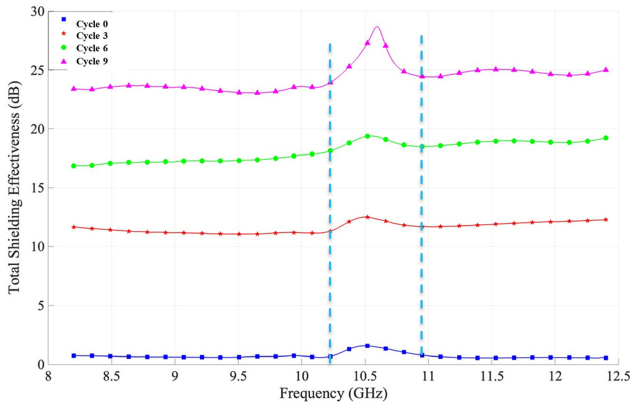

Fig. 15 Total shielding effectiveness *versus* frequency 3D printed PLA samples coated for 0, 3, 6, and 9 times.

The porous diamond-lattice structure, although inherently non-conductive, acts as a highly effective scaffold for coating deposition due to its large surface-area-to-volume ratio. This architectural advantage enhances scattering, reflection, and absorption by enabling multiple internal reflections and lengthening the EM propagation path.[32,115] As GNP layers become thicker and more continuous, they form conductive surfaces that enable efficient reflection and dissipative losses through ohmic heating and dielectric relaxation.[116] Together, the conductive coating and lattice-induced scattering create a hybrid shielding mechanism that leverages both geometry-driven and material-driven attenuation.

Interfacial polarization—particularly Maxwell–Wagner–Sillars (MWS) polarization—further contributes to shielding performance. The sharp conductivity contrast between PLA and GNP produces localized charge accumulation at the interface, strengthening dielectric losses and improving energy dissipation, especially at lower X-band frequencies.[109–111] Additionally, the periodic diamond-shaped pores can behave as resonant cavities, reinforcing attenuation through geometric resonance and aperture-induced scattering.[117,118] This combination of interfacial and geometric effects becomes increasingly important as the conductive network matures.

The small SE_T peak observed in the uncoated sample near 10 GHz arises solely from cavity resonance rather than intrinsic EM properties of PLA. This occurs due to confinement and partial reflection of EM waves within the lattice pores.[118] With increasing coating cycles, this resonance becomes stronger and begins to couple with natural cavity modes and Fabry–Pérot–type interference effects that are especially pronounced in partially coated structures.[29,119]

By cycle 6, SE_T reaches approximately 18–20 dB across the frequency band, indicating the formation of a continuous conductive GNP film. This level of connectivity enhances internal reflections, increases absorptive losses, and promotes more efficient wave damping. The stronger 10 GHz resonance peak at this stage likely results from the combined effects of extended propagation paths and improved energy trapping within the lattice. The pronounced increase in SE_T from cycle 3 to cycle 6 is consistent with the development of a more continuous conductive network, which enhances effective electromagnetic attenuation through improved interconnectivity and dielectric response.[109,120]

At cycle 9, SE_T increases further, accompanied by an even more intense resonance peak. The expanded GNP–PLA interfacial area strengthens MWS-driven polarization losses, while the thicker, more uniform coating enhances cavity resonance and constructive interference.[26,27,121] The slight rightward shift in the peak may be related to thickness-dependent changes in effective cavity dimensions and internal reflection pathways, influencing frequency-dependent attenuation behavior. Higher conductivity also reduces skin depth, improving absorption at elevated frequencies. Moreover, the denser GNP network facilitates faster dielectric relaxation processes, broadening the resonance peak and increasing the overall attenuation bandwidth. This progression shows that higher GNP loading promotes absorption-dominated shielding, increasing the integrated attenuation across the SE_T spectrum.[114,122,123]

For comparison, Fig. S2 shows the shielding effectiveness due to reflection (SE_R) for the same coating cycles. All curves exhibit a characteristic dip at the resonance region (10–10.5 GHz), followed by recovery at higher frequencies, further supporting the transition toward absorption-dominated shielding as the coating becomes thicker and more conductive.

While the present work focuses on a single lattice geometry, variations in lattice topology and characteristic length scales are expected to likely influence electromagnetic shielding behavior. Changes in unit-cell size or raster filament's dimensions, and printing pattern would alter electromagnetic wave propagation paths, internal scattering, and the effective interaction length within the porous structure.

From a physical perspective, architectural modifications can alter frequency-dependent attenuation behavior as well as EM waves absorption characteristics by influencing cavity dimensions, impedance transitions, and internal reflection pathways. The degree to which electromagnetic waves are confined, scattered, and dissipated depends strongly on lattice periodicity and pore geometry. A systematic investigation of lattice-dependent EMI responses represents an important direction for future work.

Table 2 summarizes the reflectance (R), transmittance (T), and absorbance (A) coefficients for samples coated with 0, 3, 6, and 9 GNP cycles. The uncoated sample (cycle 0) shows high transmittance ($T = 0.85$) and low reflectance ($R = 0.11$), as PLA closely matches the impedance of air and therefore exhibits minimal reflection or absorption.[114–116]

Table 2 Reflectance (*R*), transmittance (*T*), and absorbance (*A*) parameters for samples coated with 0, 3, 6, and 9 GNP cycles

Parameter	Cycle 0	Cycle 3	Cycle 6	Cycle 9
R	0.11	0.18	0.36	**0.59**
T	**0.85**	0.07	0.03	0.00
A	0.04	**0.75**	**0.62**	0.41

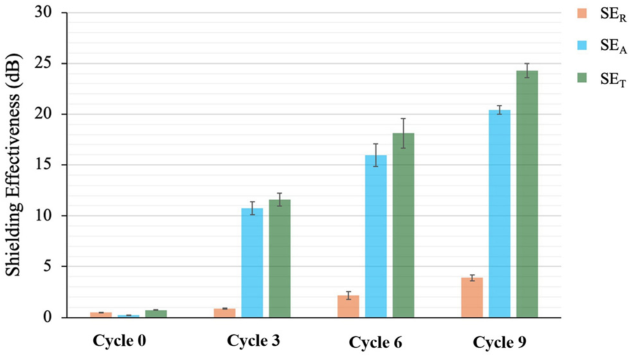

Fig. 16 Reflection, absorption, and total shielding effectiveness for 3D-printed PLA samples coated with 0, 3, 6, and 9 GNP cycles.

With increasing coating cycles, reflectance rises markedly, yet absorption remains the primary contributor to shielding. As shown in Fig. 16, shielding effectiveness due to absorption (SE_A) accounts for ~93%, 88%, and 84% of total SE_T for cycles 3, 6, and 9, respectively. Even at higher coating thicknesses, the growth in R does not translate into dominance of reflection-based shielding (SE_R).[124] Overall, the SE_R/SE_A balance remains roughly constant at ~15% and ~85%, highlighting that additional dissipation mechanisms enhance absorption beyond what surface reflectivity alone would predict. Theoretical considerations support this trend: when $R \leq 0.9$, SE_R typically remains below 10 dB.[125] whereas SE_A becomes significant once transmittance drops to $\sim 10^{-2}$ or lower—conditions met in cycles 6 and 9. This confirms that improved EMI performance at higher coating levels is governed largely by transmitted-power suppression and absorption-driven losses. Frequency-dependent R and A data (Fig. S3–S4) further show dips in reflectance and corresponding absorption peaks near 10–11 GHz.

The persistent dominance of absorption suggests that the porous lattice contributes additional attenuation pathways. According to aperture theory, the patterned geometry creates aperture-like regions that induce multiple scattering, localized resonance, and extended wave propagation paths, all of which increase the likelihood of energy dissipation.[117] When these internal pore surfaces are coated with conductive GNP, such effects intensify and broaden the absorption response across the X-band.[120]

Overall, the combined contribution of the conductive GNP coating and the finely patterned porous architecture results in absorption-dominant EMI shielding across all coating cycles. The structural design enhances electromagnetic scattering, resonance effects, and dielectric losses, leading to attenuation levels suggesting that both electrical conductivity and structural effects contribute.

Flame retardancy

Table 3 summarizes the Limiting Oxygen Index (LOI) values for 3D-printed porous PLA samples coated with 0, 3, 6, and 9 GNP dip-coating cycles. A clear and progressive enhancement in LOI is observed with increasing coating cycles. The uncoated PLA sample (cycle 0) exhibits an LOI of 19.1, confirming its high flammability. In contrast, GNP-coated samples show substantial improvements of +28.3%, +35.3%, and +43.2% for cycles 3, 6, and 9, respectively, reaching a maximum LOI of 27.5 at cycle 9. These results indicate that

Table 3 Limiting oxygen index (LOI) of 3D printed porous PLA samples coated with GNP

Material	LOI (%)
Pure PLA	19.1 ± 0.4
GNP coated PLA cycle 3	24.6 ± 0.3
GNP coated PLA cycle 6	25.9 ± 0.2
GNP coated PLA cycle 9	27.5 ± 0.2

repeated GNP dip-coating forms an increasingly effective flame-retardant barrier that delays ignition and suppresses flame spread.

LOI values are reported as mean ± standard deviation from replicate measurements.

The improved flame retardancy arises from the combined effect of the GNP coating and the diamond-shaped porous architecture. During combustion, the GNP layers facilitate the formation of a cohesive protective char that insulates the underlying polymer, slows heat transfer, and reduces pyrolysis rates.[126,127] The layered carbon network acts as an efficient thermal barrier and restricts the emission of volatile degradation products.[48]

Thermogravimetric analysis (TGA) supports this interpretation: char yield increases by 161.7%, 235.2%, and 337.1% for the 3-, 6-, and 9-cycle samples, respectively.[69] Derivative TGA (DTGA) results show broader decomposition peaks and elevated maximum decomposition temperatures ($T_{\text{d-max}}$), indicating higher thermal stability and delayed degradation.[48,127] The tortuous layered pathways created by the GNP-rich char hinder the diffusion of volatile gases and reduce their interaction with the flame front.[128,129] Additionally, GNP has been reported to impede oxygen diffusion within polymer matrices, further suppressing combustion.[130] This barrier effect is visually reflected in Fig. 10(c) and (e), where overlapping GNP sheets form a dense protective layer that limits oxygen penetration into the PLA substrate.[129]

Fig. 17 presents FESEM images of the post-combustion residues. The uncoated PLA (cycle 0) shows severe melt dripping, re-solidification, and a porous residue indicative of extensive volatile release.[131] No integrated char layer is observed. Backscattered FESEM imaging reveals scattered white regions corresponding to degradation residues enriched in barium, sulfur, and oxygen, consistent with the decomposition of PLA filaments containing barium sulfate additives.[132,133]

In contrast, GNP-coated samples exhibit markedly different combustion behavior. At cycle 3, partial char formation appears while some melt dripping persists. By cycles 6 and 9, char formation becomes dominant, effectively preserving the sample geometry. The cohesive char layer formed on the exposed walls acts as a physical barrier that prevents collapse and retains structural integrity during burning.[131]

Higher-cycle samples show better preservation of the original printing raster patterns, particularly in the central regions. Magnified backscattered images (Fig. 17b, d, f, h) confirm the presence of dense, condensed char supported by a continuous, layered GNP barrier. This structure likely contributed to limiting heat transfer, slowing combustion kinetics, and enhancing overall fire resistance.[134,135] Additional FESEM images of the residues for cycles 3, 6, and 9 are shown in Fig. S5 at various magnifications, providing further insight into the strengthened char morphology.

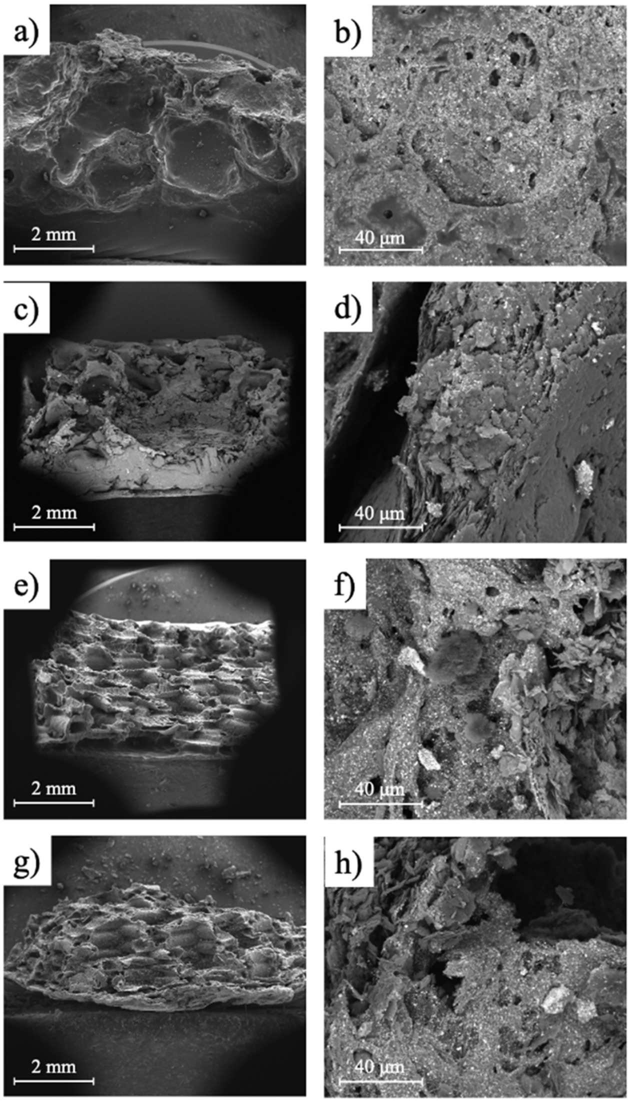

Fig. 17 FESEM images (left: secondary electron mode, right: backscattered mode) of combusted porous 3D-printed PLA samples coated with 0, 3, 6, and 9 GNP cycles. Panels (a and b) correspond to cycle 0, (c and d) to cycle 3, (e and f) to cycle 6, and (g and h) to cycle 9.

Comparison with state-of-the-art and critical perspective

The 9-cycle GNP coated lattice (total thickness ≈ 3 mm, total weight ≈ 0.6 g) exhibited an above-average total shielding effectiveness (SE_T) of ~25 dB in the X-band (8.2–12.4 GHz), with peak values approaching ~30 dB. Total shielding effectiveness equal to or above 20 dB is considered practical for most commercial electronic protection applications. normalizing the total shielding effectiveness, the thickness and weight specific total shielding performance corresponded to approximately 8 dB mm^{-1} and 42 dB g^{-1}, respectively. In many reported bulk graphene/polymer composites, comparable attenuation levels were achieved through volumetric percolation at higher filler loadings, often exceeding 10 wt%, in some cases approaching 20 wt%.[99,102,103,136] In contrast, the present architecture achieved comparable specific EMI shielding effectiveness with an estimated GNP loading of ~5.56 wt%, as determined from TGA residue analysis. This difference highlights that incorporating GNP as surface percolated networks on a lightweight 3D printed ordered lattice skeletons yields significantly superior electronic multifunctional properties compared to classic fillers dispersion within the entire polymer's volume.

Moreover, the EMI shielding mechanism was dominated by absorption, which is highly advantageous to reduce secondary electromagnetic reflection pollution and minimize potential interference with surrounding devices.[110,137–139] In this study, a periodic diamond lattice was introduced to provide abundant reflective surface areas to further attenuate EM waves intensity by absorption through internal scattering events within the porous structure. Therefore, this present study underscores the effectiveness of surface-connected conductive networks combined with architecture-mediated EM wave interactions.[32,117,119,140]

Conclusion

This study demonstrates a facile and scalable dip-coating strategy for integrating graphene nanoplatelet (GNP) surface conductive networks onto architected 3D-printed PLA lattice skeletons. The 3 mm thick structure—featuring 30% infill of a diamond lattice skeleton, with 0.9 mm unit cell size, confined by a solid wall at one side—achieved above-average total shielding effectiveness of ~25 dB (peak ~30 dB) within X-band at an estimated GNP loading of ~5.56 wt%, corresponding to 9-cycle coating, with absorption-dominant attenuation mechanism. In addition, the coated lattices achieved electrical conductivity exceeding 100 S m^{-1} and improved flame retardancy (LOI up to 27.5%), demonstrating the feasibility of combining EMI shielding, electrical conduction, and fire resistance within a single lightweight lattice platform.

The physical adhesion of GNP coating to the PLA skeleton surface was ensured by means of mechanical interlocking—surface roughening by NaOH etchant—combined with polar interfacial interactions—PEI surface conditioning. Increasing GNP coating cycles resulted in nearly linear enhancement in all multifunctional properties performances. Nevertheless, the coating peeling test results indicated that the cohesion failure between deposited GNP layers dominated the delamination mechanism as the number of coating cycles increased. Therefore, the superior multifunctional properties were traded off with a weaker coating peeling resistance, leading to choosing a non-unique number of coating cycles that suits a specific application requirement. However, 6–7 coating cycles did offer a balance between multifunctional properties, performance, and coating peeling resistance.

This study sheds light on the possible combinatorial effect of surface-percolated conductive pathways on periodic porous lattice architecture in achieving lightweight EMI shields featuring very low nanomaterial content, superior shielding effectiveness, and absorption domination.

Future work will focus on exploring how lattice topology, as well as printing parameters affect the EM waves' attenuation, impedance mismatch condition, and durability under cyclic mechanical loading to further refine architecture-enabled EMI shielding systems.

Author contributions

N. T.: conceptualization, methodology, investigation, data analysis, validation, visualization, and writing – original draft & review. M. A.: conceptualization, methodology, investigation, data analysis, validation, visualization, and writing – original draft & review. E. G. R. D. A.: methodology, investigation, data analysis, and validation. U. T.: funding acquisition, data analysis, writing – review & editing, and project supervision.

Conflicts of interest

There are no conflicts to declare.

Data availability

All data supporting the findings of this study are included within the article and its supplementary information (SI). Supplementary information is available. See DOI: https://doi.org/10.1039/d5nr05018a.

Additional raw datasets—including FESEM images, TGA/DTGA curves, LOI measurements, EMI shielding data, and electrical conductivity measurements—are available from the corresponding author upon reasonable request.

Acknowledgements

We sincerely acknowledge funding support from the Natural Science and Engineering Research Council of Canada (NSERC) Discovery Grant No. RGPIN-2020-04058 and Alberta Innovates Advance Grant 232403381. MA acknowledges the funding support provided by the Alberta Innovates Graduate Student Scholarships.

References

1 A. D. B. L. Ferreira, P. R. O. Nóvoa and A. T. Marques, Multifunctional Material Systems: A state-of-the-art review, *Compos. Struct.*, 2016, **151**, 3–35, DOI: 10.1016/J.COMPSTRUCT.2016.01.028.

2 K. Wang, K. Amin, Z. An, Z. Cai, H. Chen, H. Chen, Y. Dong, X. Feng, W. Fu, J. Gu, Y. Han, D. Hu, R. Hu, D. Huang, F. Huang, F. Huang, Y. Huang, J. Jin, X. Jin, Q. Li, T. Li, Z. Li, Z. Li, J. Liu, J. Liu, S. Liu, H. Peng, A. Qin, X. Qing, Y. Shen, J. Shi, X. Sun, B. Tong, B. Wang, H. Wang, L. Wang, S. Wang, Z. Wei, T. Xie, C. Xu, H. Xu, Z. K. Xu, B. Yang, Y. Yu, X. Zeng, X. Zhan, G. Zhang, J. Zhang, M. Q. Zhang, X. Z. Zhang, X. Zhang, Y. Zhang, Y. Zhang, C. Zhao, W. Zhao, Y. Zhou, Z. Zhou, J. Zhu,

X. Zhu and B. Z. Tang, Advanced functional polymer materials, *Mater. Chem. Front*, 2020, **4**, 1803–1915, DOI: 10.1039/D0QM00025F.

3 P. T. Curtis, Multifunctional polymer composites, *Adv. Perform. Mater.*, 1996, **3**, 279–293, DOI: 10.1007/BF00136792/METRICS.

4 Y. Zhang, G. Shen, S. S. Lam, S. Ansar, S. C. Jung, S. Ge, L. Hou, Z. Fan, F. Wang and W. Fan, A waste textiles-based multilayer composite fabric with superior electromagnetic shielding, infrared stealth and flame retardance for military applications, *Chem. Eng. J.*, 2023, **471**, 144679, DOI: 10.1016/J.CEJ.2023.144679.

5 T. S. Williams, Multifunctional Polymers and Composites for Aerospace Applications, (2019). https://www.nasa.gov (accessed March 10, 2025).

6 K. Salonitis, J. Pandremenos, J. Paralikas and G. Chryssolouris, Multifunctional Materials Used in Automotive Industry: A Critical Review, Engineering Against Fracture – Proceedings of the 1st Conference (2009) pp. 59–70. DOI: 10.1007/978-1-4020-9402-6_5.

7 Q. Guo, J. Guo, H. Chen, P. Zhou, C. Li, K. Yang, N. Hua, J. Wang and M. Weng, Multi-functional graphene/leather for versatile wearable electronics, *J. Mater. Chem. A*, 2023, **11**, 11773–11785, DOI: 10.1039/D3TA01087B.

8 W. Zhai, C. Wang, S. Wang, J. Li, Y. Zhao, P. Zhan, K. Dai, G. Zheng, C. Liu and C. Shen, Ultra-stretchable and multifunctional wearable electronics for superior electromagnetic interference shielding, electrical therapy and biomotion monitoring, *J. Mater. Chem. A*, 2021, **9**, 7238–7247, DOI: 10.1039/D0TA10991F.

9 J. Xiong, X. Zhao, Z. Liu, H. Chen, Q. Yan, H. Lian, Y. Chen, Q. Peng and X. He, Multifunctional Nacre-Like Nanocomposite Papers for Electromagnetic Interference Shielding via Heterocyclic Aramid/MXene Template-Assisted *In situ* Polypyrrole Assembly, *Nano-Micro Lett.*, 2025, **17**, 1–18, DOI: 10.1007/S40820-024-01552-9/FIGURES/8.

10 J. W. Li, C. C. Cheng and C. W. Chiu, Advances in Multifunctional Polymer-Based Nanocomposites, *Polymers*, 2024, **16**, 3440, DOI: 10.3390/POLYM16233440.

11 L. Yu, R. Peng, G. Rivers, C. Zhang, P. Si and B. Zhao, Multifunctional liquid crystal polymer network soft actuators, *J. Mater. Chem. A*, 2020, **8**, 3390–3396, DOI: 10.1039/C9TA12139K.

12 S. Ganguly and S. Margel, Fabrication and Applications of Magnetic Polymer Composites for Soft Robotics, *Micromachines*, 2023, **14**, 2173, DOI: 10.3390/MI14122173.

13 F. Signori, R. Solaro, E. Chiellini, P. A. M. Lips, P. J. Dijkstra and J. Feijen, Multifunctional polyesters as new candidate materials for biomedical applications, Synthesis and structural characterization, *Macromol. Symp.*, 2003, **197**, 289–302, DOI: 10.1002/MASY.200350726.

14 X. Y. Wang, S. Y. Liao, Y. J. Wan, P. L. Zhu, Y. G. Hu, T. Zhao, R. Sun and C. P. Wong, Electromagnetic interference shielding materials: recent progress, structure design, and future perspective, *J. Mater. Chem. C*, 2021, **10**, 44–72, DOI: 10.1039/D1TC04702G.

15 E. Erfanian, R. Moaref, R. Ajdary, K. C. Tam, O. J. Rojas, M. Kamkar and U. Sundararaj, Electrochemically synthesized graphene/TEMPO-oxidized cellulose nanofibrils hydrogels: Highly conductive green inks for 3D printing of robust structured EMI shielding aerogels, *Carbon*, 2023, **210**, 118037, DOI: 10.1016/J.CARBON.2023.118037.

16 H. K. Choudhary, R. Kumar, S. P. Pawar, U. Sundararaj and B. Sahoo, Superiority of graphite coated metallic-nanoparticles over graphite coated insulating-nanoparticles for enhancing EMI shielding, *New J. Chem.*, 2021, **45**, 4592–4600, DOI: 10.1039/D0NJ06231F.

17 M. Daniela Falco, D. Genovesi, L. Caravatta, C. Di Carlo, E. Bliakharskaia, M. Appignani, M. Faustino, N. Furia and E. Di Girolamo, A randomized in vitro evaluation of transient and permanent cardiac implantable electronic device malfunctions following direct exposure up to 10 Gy, (n.d.). DOI: 10.1007/s00066-020-01651-7.

18 P. M. Mariappan, D. Raghavan, S. H. E. Abdel Aleem and A. F. Zobaa, Effects of electromagnetic interference on the functional usage of medical equipment by 2G/3G/4G cellular phones: A review, *J. Adv. Res.*, 2016, **7**, 727–738, DOI: 10.1016/j.jare.2016.04.004.

19 Y. Stein, O. Hänninen, P. Huttunen, M. Ahonen and R. Ekman, Electromagnetic Radiation and Health: Human Indicators, *Environ. Indic.*, 2015, 1025–1046, DOI: 10.1007/978-94-017-9499-2_57.

20 D. Schuermann and M. Mevissen, Manmade Electromagnetic Fields and Oxidative Stress—Biological Effects and Consequences for Health, *Int. J. Mol. Sci.*, 2021, **22**, 3772, DOI: 10.3390/ijms22073772.

21 F. Deruelle, The different sources of electromagnetic fields: Dangers are not limited to physical health, *Electromagn. Biol. Med.*, 2020, **39**, 166–175, DOI: 10.1080/15368378.2020.1737811.

22 J. Kruželák, A. Kvasničáková, K. Hložeková and I. Hudec, Progress in polymers and polymer composites used as efficient materials for EMI shielding, *Nanoscale Adv.*, 2021, **3**, 123–172, DOI: 10.1039/D0NA00760A.

23 A. Meher, B. B. Sahu, R. N. Mahaling, S. Sagadevan and S. Moharana, Polymer Composites for Electromagnetic Interference (EMI), Shielding Applications, *Eng. Mater.*, 2024, **2024**, 459–488, DOI: 10.1007/978-981-97-2075-0_15.

24 A. S. Husein, *Theoretical Analysis of Reflection and Refraction of Electromagnetic Waves on an Anisotropic, Inhomogeneous and Linear Medium.* ArXiv (Cornell University), 2012.

25 J. Bi, Z. Sun, Z. Guo, S. Tian, G. Li and L. Qian, Negative permittivity enhanced reflection and adsorption of electromagnetic waves from carbon fiber felt/carbon nanotubes, *J. Mater. Chem. C*, 2024, **12**, 13974–13984, DOI: 10.1039/D4TC02961E.

26 *Advanced Materials for Electromagnetic Shielding*, ed. M. Jaroszewski, S. Thomas and A. V. Rane, 2018. DOI: 10.1002/9781119128625.

27 A. A. Isari, A. Ghaffarkhah, S. A. Hashemi, S. Wuttke and M. Arjmand, Structural Design for EMI Shielding: From Underlying Mechanisms to Common Pitfalls, *Adv. Mater.*, 2024, **36**, 2310683, DOI: 10.1002/ADMA.202310683.

28 Y. Du, Y. Liu, A. Wang and J. Kong, Research progress and future perspectives on electromagnetic wave absorption of fibrous materials, *iScience*, 2023, **26**, 107873, DOI: 10.1016/J.ISCI.2023.107873.

29 Y. Gao and Z. Wang, Microwave absorption and electromagnetic interference shielding properties of Li-Zn ferrite-carbon nanotubes composite, *J. Magn. Magn. Mater.*, 2021, **528**, 167808, DOI: 10.1016/J.JMMM.2021.167808.

30 B. Ribeiro, N. A. S. Gomes, M. Baldan and M. C. Rezende, Designing Sandwich Architecture Towards Glass Fiber/Epoxy Reinforced Multi-walled Carbon Nanotube Buckypaper Composites for Electromagnetic Interference Shielding, *Electron. Mater. Lett.*, 2022, **19**, 184–191, DOI: 10.1007/S13391-022-00382-4.

31 W. L. Song, L. Z. Fan, M. S. Cao, M. M. Lu, C. Y. Wang, J. Wang, T. T. Chen, Y. Li, Z. L. Hou, J. Liu and Y. P. Sun, Facile fabrication of ultrathin graphene papers for effective electromagnetic shielding, *J. Mater. Chem. C*, 2014, **2**, 5057–5064, DOI: 10.1039/C4TC00517A.

32 Q. Lv, Z. Peng, H. Pei, X. Zhang, Y. Chen, H. Zhang, X. Zhu and S. Wu, 3D Printing of Periodic Porous Metamaterials for Tunable Electromagnetic Shielding Across Broad Frequencies, *Nano-Micro Lett.*, 2024, **16**, 1–20, DOI: 10.1007/S40820-024-01502-5/FIGURES/7.

33 J. Shen, J. Liang, X. Lin, H. Lin, J. Yu and S. Wang, The Flame-Retardant Mechanisms and Preparation of Polymer Composites and Their Potential Application in Construction Engineering, *Polymers*, 2021, **14**, 82, DOI: 10.3390/POLYM14010082.

34 A. Dasari, Z. Z. Yu, G. P. Cai and Y. W. Mai, Recent developments in the fire retardancy of polymeric materials, *Prog. Polym. Sci.*, 2013, **38**, 1357–1387, DOI: 10.1016/j.progpolymsci.2013.06.006.

35 K. K. Shen, S. Kochesfahani and F. Jouffret, Zinc borates as multifunctional polymer additives, *Polym. Adv. Technol.*, 2008, **19**, 469–474, DOI: 10.1002/PAT.1119.

36 J. Yan, M. Chen, R. Tan, C. Lin, S. Jiang, W. Wang, S. Pan, H. Xiao, E. Ren and R. Guo, Flexible multifunctional MXene@Ag nanowires/cotton fabric inspired by transport of nutrients by roots for electromagnetic shielding, infrared stealth, Joule/solar heating and flame retardancy, *J. Mater. Chem. A*, 2024, **12**, 33162–33176, DOI: 10.1039/D4TA06712F.

37 Q. Yu, W. Han, L. Qiu, Y. Yu, L. Yi and D. Chen, Exceptionally flame retardant and electromagnetic interference shielding aramid nanofiber-Ti3C2Tx MXene twin-layered films with remarkable mechanical strength and flexibility, *J. Alloys Compd.*, 2024, **1000**, 175119, DOI: 10.1016/J.JALLCOM.2024.175119.

38 V. K. Chakradhary, S. Gangwar, M. J. Akhtar, K. K. Kar and S. Jha, Design of Flame-Retardant, Hydrophobic, Ultrathin, Lightweight and Flexible EMI shielding Fabric and Sheets for Defense, Space & Industrial Applications, 2023 IEEE Microwaves, Antennas, and Propagation Conference, MAPCON 2023, 2023. DOI: 10.1109/MAPCON58678.2023.10463886.

39 X. Jin, J. Wang, L. Dai, X. Liu, L. Li, Y. Yang, Y. Cao, W. Wang, H. Wu and S. Guo, Flame-retardant poly(vinyl alcohol)/MXene multilayered films with outstanding electromagnetic interference shielding and thermal conductive performances, *Chem. Eng. J.*, 2020, **380**, 122475, DOI: 10.1016/J.CEJ.2019.122475.

40 U. Hwang, J. Lee, S. Kim, X. Yang, S. Kim, J. Suhr and J. Do Nam, Structural Design of Hybrid Fillers in a Polymer Matrix for Advanced Electromagnetic Interference Shielding, *Small Struct.*, 2025, **6**, 2400404, DOI: 10.1002/SSTR.202400404.

41 G. E. Zaikov and S. M. Lomakin, Ecological issue of polymer flame retardancy, *J. Appl. Polym. Sci.*, 2002, **86**, 2449–2462, DOI: 10.1002/APP.10946.

42 N. R. Council, Toxicological Risks of Selected Flame-Retardant Chemicals, Toxicological Risks of Selected Flame-Retardant Chemicals, 2000. DOI: 10.17226/9841.

43 X. Wang, E. N. Kalali, J. T. Wan and D. Y. Wang, Carbon-family materials for flame retardant polymeric materials, Prog, *Polym. Sci*, 2017, **69**, 22–46, DOI: 10.1016/J.PROGPOLYMSCI.2017.02.001.

44 D. R. Paul and L. M. Robeson, Polymer nanotechnology: Nanocomposites, *Polymer*, 2008, **49**, 3187–3204, DOI: 10.1016/J.POLYMER.2008.04.017.

45 G. Huang, J. Gao, X. Wang, H. Liang and C. Ge, How can graphene reduce the flammability of polymer nanocomposites?, *Mater. Lett.*, 2012, **66**, 187–189, DOI: 10.1016/J.MATLET.2011.08.063.

46 D. Hofmann, K. A. Wartig, R. Thomann, B. Dittrich, B. Schartel and R. Mülhaupt, Functionalized Graphene and Carbon Materials as Additives for Melt-Extruded Flame Retardant Polypropylene, *Macromol. Mater. Eng.*, 2013, **298**, 1322–1334, DOI: 10.1002/MAME.201200433.

47 G. Huang, S. Chen, S. Tang and J. Gao, A novel intumescent flame retardant-functionalized graphene: Nanocomposite synthesis, characterization, and flammability properties, *Mater. Chem. Phys.*, 2012, **135**, 938–947, DOI: 10.1016/J.MATCHEMPHYS.2012.05.082.

48 I. Ali, N. K. Kim and D. Bhattacharyya, Effects of Graphene Nanoplatelets on Mechanical and Fire Performance of Flax Polypropylene Composites with Intumescent Flame Retardant, *Molecules*, 2021, **26**, 4094, DOI: 10.3390/MOLECULES26134094.

49 C. I. Idumah, A. Hassan and S. Bourbigot, Influence of exfoliated graphene nanoplatelets on flame retardancy of kenaf flour polypropylene hybrid nanocomposites, *J. Anal. Appl. Pyrolysis*, 2017, **123**, 65–72, DOI: 10.1016/J.JAAP.2017.01.006.

50 S. Matta, L. G. Rizzi and A. Frache, PET Foams Surface Treated with Graphene Nanoplatelets: Evaluation of Thermal Resistance and Flame Retardancy, *Polymers*, 2021, **13**, 501, DOI: 10.3390/POLYM13040501.

51 M. J. Kim, I. Y. Jeon, J. M. Seo, L. Dai and J. B. Baek, Graphene phosphonic acid as an efficient flame retardant, *ACS Nano*, 2014, **8**, 2820–2825, DOI: 10.1021/NN4066395/SUPPL_FILE/NN4066395_SI_002.AVI.

52 K. Song, I. Ganguly, I. Eastin and A. B. Dichiara, Lignin-Modified Carbon Nanotube/Graphene Hybrid Coating as Efficient Flame Retardant, *Int. J. Mol. Sci.*, 2017, **18**, 2368, DOI: 10.3390/IJMS18112368.

53 W. Chen, P. Liu, L. Min, Y. Zhou, Y. Liu, Q. Wang and W. Duan, Non-covalently Functionalized Graphene Oxide-Based Coating to Enhance Thermal Stability and Flame Retardancy of PVA Film, *Nano-Micro Lett.*, 2018, **10**, 1–13, DOI: 10.1007/S40820-018-0190-8/FIGURES/10.

54 X. Tang and M. Zhou, MXene-based electromagnetic wave response, *J. Phys.: Energy*, 2021, **3**, 042001, DOI: 10.1088/2515-7655/abf8f7.

55 W. Zhao and Z. Wang, Adhesion improvement of electroless copper to PC substrate by a low environmental pollution MnO$_2$–H3PO4–H$_2$SO4–H$_2$O system, *Int. J. Adhes. Adhes.*, 2013, **41**, 50–56, DOI: 10.1016/J.IJADHADH.2012.10.002.

56 P. Slepicka, I. Michaljaničová, N. Slepickova Kasalkova, Z. Kolská, S. Rimpelová, T. Ruml and V. Švorčík, Poly-l-lactic acid modified by etching and grafting with gold nanoparticles, *J. Mater. Sci.*, 2013, **48**, 5871–5879, DOI: 10.1007/s10853-013-7383-9.

57 V. Swarnalatha, S. Purohit, P. Pal and R. K. Sharma, Enhanced etching characteristics of Si{100} in NaOH-based two-component solution, *Micro Nano Syst. Lett.*, 2022, **10**, 1–8, DOI: 10.1186/S40486-022-00152-9/FIGURES/9.

58 T. Kim and J. Yi, Application of hydrophobic coating to reduce leakage current through surface energy control of high voltage insulator, *Appl. Surf. Sci.*, 2022, **578**, 151820, DOI: 10.1016/J.APSUSC.2021.151820.

59 W. Zhao and Z. Wang, Adhesion improvement of electroless copper to PC substrate by a low environmental pollution MnO$_2$–H3PO4–H$_2$SO4–H$_2$O system, *Int. J. Adhes. Adhes.*, 2013, **41**, 50–56, DOI: 10.1016/J.IJADHADH.2012.10.002.

60 C. Vallés, X. Zhang, J. Cao, F. Lin, R. J. Young, A. Lombardo, A. C. Ferrari, L. Burk, R. Mülhaupt and I. A. Kinloch, Graphene/Polyelectrolyte Layer-by-Layer Coatings for Electromagnetic Interference Shielding, *ACS Appl. Nano Mater.*, 2019, **2**, 5272–5281, DOI: 10.1021/ACSANM.9B01126/ASSET/IMAGES/MEDIUM/AN-2019-011268_M003.GIF.

61 W. Chen, P. Liu, L. Min, Y. Zhou, Y. Liu, Q. Wang and W. Duan, Non-covalently Functionalized Graphene Oxide-Based Coating to Enhance Thermal Stability and Flame Retardancy of PVA Film, *Nano-Micro Lett.*, 2018, **10**, 1–13, DOI: 10.1007/S40820-018-0190-8/FIGURES/10.

62 T. Kim and J. Yi, Application of hydrophobic coating to reduce leakage current through surface energy control of high voltage insulator, *Appl. Surf. Sci.*, 2022, **578**, 151820, DOI: 10.1016/J.APSUSC.2021.151820.

63 Test Methods for Rating Adhesion by Tape Test, 2017. DOI: 10.1520/D3359-17.

64 N. Demarquette, M.-C. Heuzey, M. Kontopoulou, R. Moaref, S. Shajari and U. Sundararaj, From Waste to Value Added Products: Manufacturing High Electromagnetic Interference Shielding Composite from End-of-Life Vehicle (ELV) Waste, *Polymers*, 2023, **16**, 120, DOI: 10.3390/POLYM16010120.

65 H. Wang, S. Li, M. Liu, J. Li and X. Zhou, Review on Shielding Mechanism and Structural Design of Electromagnetic Interference Shielding Composites, *Macromol. Mater. Eng.*, 2021, **306**, 2100032, DOI: 10.1002/MAME.202100032;WGROUP:STRING:PUBLICATION.

66 H. Zou, C. Yi, L. Wang, H. Liu and W. Xu, Thermal degradation of poly(lactic acid) measured by thermogravimetry coupled to Fourier transform infrared spectroscopy, *J. Therm. Anal. Calorim.*, 2009, **97**, 929–935, DOI: 10.1007/S10973-009-0121-5/FIGURES/6.

67 B. W. Chieng, N. A. Ibrahim, W. M. Z. W. Yunus, M. Z. Hussein and Y. Y. Loo, Effect of graphene nanoplatelets as nanofiller in plasticized poly(lactic acid) nanocomposites: Thermal properties and mechanical properties, *J. Therm. Anal. Calorim.*, 2014, **118**, 1551–1559, DOI: 10.1007/s10973-014-4084-9.

68 G. Manasoglu, R. Celen, M. Kanik and Y. Ulcay, An Investigation on the Thermal and Solar Properties of Graphene-Coated Polyester Fabrics, *Coatings*, 2021, **11**, 125, DOI: 10.3390/COATINGS11020125.

69 G. Schinazi, E. J. Price and D. A. Schiraldi, Fire testing methods of bio-based flame-retardant polymeric materials, in *Bio-Based Flame-Retardant Technology for Polymeric Materials*, 2022, pp. 61–95. DOI: 10.1016/B978-0-323-90771-2.00009-2.

70 K. L. Cheong, M. M. Pang, J. H. Low, K. Y. Tshai, S. C. Koay, W. Y. Wong, S. Y. Ch'ng and Y. F. Buys, Graphene Nanoplatelets/Polylactic Acid Conductive Polymer Composites: Tensile, Thermal and Electrical Properties, *Chem. Eng. Technol.*, 2024, **47**, e202300592, DOI: 10.1002/CEAT.202300592.

71 K. Maghsoudi, G. Momen and R. Jafari, The thermodynamic stability of the Cassie–Baxter regime determined by the geometric parameters of hierarchical superhydrophobic surfaces, *Appl. Mater. Today*, 2023, **34**, 101893, DOI: 10.1016/J.APMT.2023.101893.

72 C. A. J. Richards, C. F. Glover, G. Williams, H. N. McMurray and J. Baker, Evaluation of multi-layered graphene nano-platelet composite coatings for corrosion control part I - contact potentials and gas permeability, Corros, *Sci*, 2018, **136**, 285–291, DOI: 10.1016/J.CORSCI.2018.03.016.

73 Q. Sun, Y. N. Chen and Y. Z. Liu, Wetting Transition from Wenzel to Cassie States: Thermodynamic Analysis, *Materials*, 2025, **18**, 543, DOI: 10.3390/MA18030543/S1.

74 R. Yang, S. Zuo, B. Song, H. Mao, Z. Huang, Y. Wu, L. Cai, S. Ge, H. Lian and C. Xia, Hollow Mesoporous Microspheres Coating for Super-Hydrophobicity Wood

with High Thermostability and Abrasion Performance, *Polymers*, 2020, **12**, 2856, DOI: 10.3390/POLYM12122856.

75 Y. Zhang, S. Tang, D. Deng, S. Deng, J. Chen and N. Xu, Growth direction manipulation of few-layer graphene in the vertical plane with parallel arrangement, *Carbon*, 2013, **56**, 103–108, DOI: 10.1016/J.CARBON.2012.12.078.

76 S. G. Prolongo, R. Moriche, M. Sánchez and A. Ureña, Self-stratifying and orientation of exfoliated few-layer graphene nanoplatelets in epoxy composites, *Compos. Sci. Technol.*, 2013, **85**, 136–141, DOI: 10.1016/J.COMPSCITECH.2013.06.015.

77 D. Qu, R. Suter and S. Garoff, Surfactant self-assemblies controlling spontaneous dewetting, *Langmuir*, 2002, **18**, 1649–1654, DOI: 10.1021/LA011237R/ASSET/IMAGES/LARGE/LA011237RF00007.JPEG.

78 K. Afanasiev, A. Münch and B. Wagner, Landau-Levich problem for non-Newtonian liquids, *Phys. Rev. E: Stat., Nonlinear, Soft Matter Phys.*, 2007, **76**, 036307, DOI: 10.1103/PHYSREVE.76.036307/DELIVERABLE/AB173331-3B07-439F-B1BB-43AD78BEE98E.

79 L. Landau and B. Levich, Dragging of a Liquid by a Moving Plate, in *Dynamics of Curved Fronts*, 1988, pp. 141–153. DOI: 10.1016/B978-0-08-092523-3.50016-2.

80 D. Quéré, Fluid coating on a fiber, *Annu. Rev. Fluid Mech.*, 1999, **31**, 347–384, DOI: 10.1146/ANNUREV.FLUID.31.1.347/CITE/REFWORKS.

81 S. Palma and H. Lhuissier, Dip-coating with a particulate suspension, *J. Fluid Mech.*, 2019, **869**, R3, DOI: 10.1017/JFM.2019.267.

82 J. Payandehpeyman, M. Mazaheri, A. S. Zeraati, S. Jamasb and U. Sundararaj, Physics-Based Modeling and Experimental Study of Conductivity and Percolation Threshold in Carbon Black Polymer Nanocomposites, *Appl. Compos. Mater.*, 2024, **31**, 127–147, DOI: 10.1007/S10443-023-10169-X/FIGURES/7.

83 M. Mazaheri, J. Payandehpeyman and S. Jamasb, Modeling of Effective Electrical Conductivity and Percolation Behavior in Conductive-Polymer Nanocomposites Reinforced with Spherical Carbon Black, *Appl. Compos. Mater.*, 2022, **29**, 695–710, DOI: 10.1007/S10443-021-09991-Y/FIGURES/4.

84 H. Kim, F. Boulogne, E. Um, I. Jacobi, E. Button and H. A. Stone, Controlled Uniform Coating from the Interplay of Marangoni Flows and Surface-Adsorbed Macromolecules, *Phys. Rev. Lett.*, 2016, **116**, 124501, DOI: 10.1103/PHYSREVLETT.116.124501/REVISED_SUPPORTING_INFORMATION.PDF.

85 M. Ubaidullah, M. Mehmood, M. T. Tanvir, T. Ghani, A. Mahmood, A. Shah and Y. Khan, Preparation of composite-layered structure of TiO2 nanoparticles/TiO2 nanotubes and its role in dye sensitized solar cell, *J. Porous Mater.*, 2021, **28**, 555–566, DOI: 10.1007/S10934-020-00975-0/TABLES/2.

86 F. Xiang, D. Parviz, T. M. Givens, P. Tzeng, E. M. Davis, C. M. Stafford, M. J. Green and J. C. Grunlan, Stiff and Transparent Multilayer Thin Films Prepared Through Hydrogen-Bonding Layer-by-Layer Assembly of Graphene and Polymer, *Adv. Funct. Mater.*, 2016, **26**, 2143–2149, DOI: 10.1002/ADFM.201504758.

87 J. Ding, H. Zhao and H. Yu, Superior and durable graphene-based composite coatings by bioinspired interfaces and alignment, *Compos. Sci. Technol.*, 2021, **214**, 108967, DOI: 10.1016/J.COMPSCITECH.2021.108967.

88 B. Shen, Y. Li, D. Yi, W. Zhai, X. Wei and W. Zheng, Microcellular graphene foam for improved broadband electromagnetic interference shielding, *Carbon*, 2016, **102**, 154–160, DOI: 10.1016/J.CARBON.2016.02.040.

89 H. Kim, A. A. Abdala and C. W. MacOsko, Graphene/polymer nanocomposites, *Macromolecules*, 2010, **43**, 6515–6530, DOI: 10.1021/MA100572E/ASSET/IMAGES/LARGE/MA-2010-00572E_0015.JPEG.

90 S. W. Lee, K. K. Kim, Y. Cui, S. C. Lim, Y. W. Cho, S. M. Kim and Y. H. Lee, Adhesion test of carbon nanotube film coated onto transparent conducting substrates, *Nano*, 2010, **5**, 133–138, DOI: 10.1142/S1793292010002025/ASSET/IMAGES/LARGE/S1793292010002025.JPEG.

91 T. B. Yallew, P. Narute, R. S. Sharbidre, J. C. Byen, J. Park and S. G. Hong, Effects of the Transfer Method and Interfacial Adhesion on the Frictional and Wear Resistance Properties of a Graphene-Coated Polymer, *Nanomaterials*, 2023, **13**, 655, DOI: 10.3390/NANO13040655/S1.

92 Z. Wu, Y. Shen, J. Tao, Z. Jia, H. Chen, J. Jiang and Z. Wang, Green Synthesis of Mechanical Robust Superhydrophobic CNT@PU Coatings with High Flexibility for Extensive Applications, *J. Bionic Eng.*, 2021, **18**, 40–54, DOI: 10.1007/S42235-021-0016-0/METRICS.

93 W. K. Kuo, S. C. Huang and H. H. Yu, Preparation of carbon nanotubes as the conductive coating layer on flexible thermal-resistant substrate by permeating method and its residual stress analysis, *Appl. Phys. A: Mater. Sci. Process.*, 2014, **114**, 1167–1173, DOI: 10.1007/S00339-013-7709-0/FIGURES/9.

94 S. He, J. Zhang, X. Xiao, X. Hong and Y. Lai, Investigation of the conductive network formation of polypropylene/graphene nanoplatelets composites for different platelet sizes, *J. Mater. Sci.*, 2017, **52**, 13103–13119, DOI: 10.1007/S10853-017-1413-Y/FIGURES/12.

95 E. Erfanian, M. Kamkar, S. P. Pawar, Y. Zamani Keteklahijani, M. Arjmand and U. Sundararaj, A Simple Approach to Control the Physical and Chemical Features of Custom-Synthesized N-Doped Carbon Nanotubes and the Extent of Their Network Formation in Polymers: The Importance of Catalyst to Substrate Ratio, *Polymers*, 2021, **13**, 4156, DOI: 10.3390/POLYM13234156.

96 R. Moriche, M. A. Moreno-Avilés, A. Jiménez-Suárez, S. G. Prolongo and A. Ureña, Graphene nanoplatelets electrical networks as highly efficient self-heating materials for glass fiber fabrics, *J. Ind. Text.*, 2022, **51**, 4410S–4423S, DOI: 10.1177/1528083720931482/ASSET/8956D4FC-FB88-49B9-8C5E-A575E0E62AE8/ASSETS/IMAGES/LARGE/10.1177_1528083720931482-FIG8.JPG.

97 T. W. Lee, S. E. Lee and Y. G. Jeong, Carbon nanotube/cellulose papers with high performance in electric heating and electromagnetic interference shielding, *Compos. Sci. Technol.*, 2016, **131**, 77–87, DOI: 10.1016/J.COMPSCITECH.2016.06.003.

98 H. Souri and D. Bhattacharyya, Electrical conductivity of the graphene nanoplatelets coated natural and synthetic fibres using electrophoretic deposition technique, *Int. J. Smart Nano Mater.*, 2018, **9**, 167–183, DOI: 10.1080/19475411.2018.1476419.

99 M. Tian, R. Zhao, L. Qu, Z. Chen, S. Chen, S. Zhu, W. Song, X. Zhang, Y. Sun and R. Fu, Stretchable and Designable Textile Pattern Strain Sensors Based on Graphene Decorated Conductive Nylon Filaments, *Macromol. Mater. Eng.*, 2019, **304**, 1900244, DOI: 10.1002/MAME.201900244.

100 P. Cataldi, L. Ceseracciu, S. Marras, A. Athanassiou and I. S. Bayer, Electrical conductivity enhancement in thermoplastic polyurethane-graphene nanoplatelet composites by stretch-release cycles, *Appl. Phys. Lett.*, 2017, **110**, 121904, DOI: 10.1063/1.4978865/33217.

101 B. Zhao, C. Zhao, M. Hamidinejad, C. Wang, R. Li, S. Wang, K. Yasamin and C. B. Park, Incorporating a microcellular structure into PVDF/graphene–nanoplatelet composites to tune their electrical conductivity and electromagnetic interference shielding properties, *J. Mater. Chem. C*, 2018, **6**, 10292–10300, DOI: 10.1039/C8TC03714K.

102 N. A. Masarra, M. Batistella, J. C. Quantin, A. Regazzi, M. F. Pucci, R. El Hage and J. M. Lopez-Cuesta, Fabrication of PLA/PCL/Graphene Nanoplatelet (GNP) Electrically Conductive Circuit Using the Fused Filament Fabrication (FFF) 3D Printing Technique, *Materials*, 2022, **15**, 762, DOI: 10.3390/MA15030762.

103 Y. Gao, O. T. Picot, E. Bilotti and T. Peijs, Influence of filler size on the properties of poly(lactic acid) (PLA)/graphene nanoplatelet (GNP) nanocomposites, *Eur. Polym. J.*, 2017, **86**, 117–131, DOI: 10.1016/J.EURPOLYMJ.2016.10.045.

104 A. Paydayesh, F. Pashaei Soorbaghi, A. Aref Azar and A. Jalali-Arani, Electrical conductivity of graphene filled PLA/PMMA blends: Experimental investigation and modeling, *Polym. Compos.*, 2018, **40**, 704–715, DOI: 10.1002/PC.24722.

105 X. Zheng, P. Wang, X. Zhang, Q. Hu, Z. Wang, W. Nie, L. Zou, C. Li and X. Han, Breathable, durable and bark-shaped MXene/textiles for high-performance wearable pressure sensors, EMI shielding and heat physiotherapy, *Composites, Part A*, 2022, **152**, 106700, DOI: 10.1016/J.COMPOSITESA.2021.106700.

106 G. Wang, Z. Gao, S. Tang, C. Chen, F. Duan, S. Zhao, S. Lin, Y. Feng, L. Zhou and Y. Qin, Microwave absorption properties of carbon nanocoils coated with highly controlled magnetic materials by atomic layer deposition, *ACS Nano*, 2012, **6**, 11009–11017, DOI: 10.1021/NN304630H/SUPPL_FILE/NN304630H_SI_001.PDF.

107 G. Mutlu, F. Yıldırım, H. Ulus and V. Eskizeybek, Coating graphene nanoplatelets onto carbon fabric with controlled thickness for improved mechanical performance and EMI shielding effectiveness of carbon/epoxy composites, *Eng. Fract. Mech.*, 2023, **284**, 109271, DOI: 10.1016/J.ENGFRACMECH.2023.109271.

108 H. Gao, C. Wang, Z. Yang and Y. Zhang, 3D porous nickel metal foam/polyaniline heterostructure with excellent electromagnetic interference shielding capability and superior absorption based on pre-constructed macroscopic conductive framework, *Compos. Sci. Technol.*, 2021, **213**, 108896, DOI: 10.1016/J.COMPSCITECH.2021.108896.

109 X. Xia, Y. Wang, Z. Zhong and G. J. Weng, A theory of electrical conductivity, dielectric constant, and electromagnetic interference shielding for lightweight graphene composite foams, *J. Appl. Phys.*, 2016, **120**, 85102, DOI: 10.1063/1.4961401/13988897/085102_1_ACCEPTED_MANUSCRIPT.PDF.

110 B. Wang, H. Wu, W. Hou, Z. Fang, H. Liu, F. Huang, S. Li and H. Zhang, Optimizing dielectric polarization for electromagnetic wave attenuation via an enhanced Maxwell–Wagner–Sillars effect in hollow carbon microspheres, *J. Mater. Chem. A*, 2023, **11**, 23498–23510, DOI: 10.1039/D3TA05647C.

111 F. Pan, L. Cai, Y. Shi, Y. Dong, X. Zhu, J. Cheng, H. Jiang, X. Wang, Y. Jiang and W. Lu, Heterointerface Engineering of β-Chitin/Carbon Nano-Onions/Ni–P Composites with Boosted Maxwell-Wagner-Sillars Effect for Highly Efficient Electromagnetic Wave Response and Thermal Management, *Nano-Micro Lett.*, 2022, **14**, 1–18, DOI: 10.1007/S40820-022-00804-W/FIGURES/9.

112 L. Wang, Z. Xie, Y. Zhan, X. Hao, Y. Meng, S. Wei, Z. Chen and H. Xia, Robust, flexible, and high-performance electromagnetic interference shielding films with long-lasting service, *RSC Adv.*, 2021, **11**, 18476–18482, DOI: 10.1039/D1RA02756E.

113 J. Li, L. Wang, H. Luo, Q. Gao, Y. Chen, J. Xiang, J. Yan and H. Fan, Sandwich-like high-efficient EMI shielding materials based on 3D conductive network and porous microfiber skeleton, *Colloids Surf., A*, 2022, **655**, 130163, DOI: 10.1016/J.COLSURFA.2022.130163.

114 J. H. Park, J. Park, F. Tang, Y. G. Song and Y. G. Jeong, Electromagnetic Interference Shielding and Joule Heating Properties of Flexible, Lightweight, and Hydrophobic MXene/Nickel-Coated Polyester Fabrics Manufactured by Dip-Dry Coating and Electroless Plating, *ACS Appl. Mater. Interfaces*, 2024, **16**, 38490–38500, DOI: 10.1021/ACSAMI.4C06735/SUPPL_FILE/AM4C06735_SI_001.PDF.

115 H. Gao, C. Wang, Z. Yang and Y. Zhang, 3D porous nickel metal foam/polyaniline heterostructure with excellent electromagnetic interference shielding capability and superior absorption based on pre-constructed macroscopic conductive framework, *Compos. Sci. Technol.*, 2021, **213**, 108896, DOI: 10.1016/J.COMPSCITECH.2021.108896.

116 B. Salahuddin, S. N. Faisal, T. A. Baigh, M. N. Alghamdi, M. S. Islam, B. Song, X. Zhang, S. Gao and S. Aziz,

Carbonaceous Materials Coated Carbon Fibre Reinforced Polymer Matrix Composites, *Polymers*, 2021, **13**, 2771, DOI: 10.3390/POLYM13162771.

117 I. B. Başyiğit and M. F Çağlar, Comprehensive analysis of shielding effectiveness of enclosures with apertures: Parametrical approach, *Prog. Electromagn. Res. C*, 2016, **70**, 9–22, DOI: 10.2528/PIERC16072503.

118 Z. Kubík and J. Skála, Influence of the cavity resonance on shielding effectiveness of perforated shielding boxes, International Conference-Workshop Compatibility in Power Electronics, CPE (2013) pp. 260–263. DOI: 10.1109/CPE.2013.6601166.

119 G. Alagappan, F. J. García-Vidal and C. E. Png, Fabry-Perot Resonances in Bilayer Metasurfaces, *Phys. Rev. Lett.*, 2024, **133**, 226901, DOI: 10.1103/PHYSREVLETT.133.226901/SUPPLEMENTAL_MATERIAL_REVISED.PDF.

120 T. Wu, X. Huan, H. Zhang, L. Wu, G. Sui and X. Yang, The orientation and inhomogeneous distribution of carbon nanofibers and distinctive internal structure in polymer composites induced by 3D-printing enabling electromagnetic shielding regulation, *J. Colloid Interface Sci.*, 2023, **638**, 392–402, DOI: 10.1016/J.JCIS.2023.02.014.

121 G. M. Mamatha, P. Dixit, R. H. Krishna and S. Girish Kumar, Polymer based composites for electromagnetic interference (EMI) shielding: The role of magnetic fillers in effective attenuation of microwaves, a review, *Hybrid Adv.*, 2024, **6**, 100200, DOI: 10.1016/J.HYBADV.2024.100200.

122 A. Iqbal, P. Sambyal and C. Min Koo, 2D MXenes for Electromagnetic Shielding, A Review, *Adv. Funct. Mater.*, 2020, **30**, 2000883, DOI: 10.1002/ADFM.202000883.

123 J. Wang, F. Wu, Y. Cui, A. Zhang, Q. Zhang and B. Zhang, Efficient synthesis of N-doped porous carbon nanoribbon composites with selective microwave absorption performance in common wavebands, *Carbon*, 2021, **175**, 164–175, DOI: 10.1016/J.CARBON.2021.01.005.

124 M. Peng and F. Qin, Clarification of basic concepts for electromagnetic interference shielding effectiveness, *J. Appl. Phys.*, 2021, **130**, 2251108, DOI: 10.1063/5.0075019/158414.

125 S. H. Ryu, Y. K. Han, S. J. Kwon, T. Kim, B. M. Jung, S. B. Lee and B. Park, Absorption-dominant, low reflection EMI shielding materials with integrated metal mesh/TPU/CIP composite, *Chem. Eng. J.*, 2022, **428**, 131167, DOI: 10.1016/J.CEJ.2021.131167.

126 Y. Yu, Y. Zhang, L. Xi, Z. Zhao, S. Huo, G. Huang, Z. Fang and P. Song, Interface nanoengineering of a core-shell structured biobased fire retardant for fire-retarding polylactide with enhanced toughness and UV protection, *J. Cleaner Prod*, 2022, **336**, 130372, DOI: 10.1016/J.JCLEPRO.2022.130372.

127 L. T. Temane, S. S. Ray and J. T. Orasugh, Review on Processing, Flame-Retardant Properties, and Applications of Polyethylene Composites with Graphene-Based Nanomaterials, *Macromol. Mater. Eng.*, 2024, **309**, 2400104, DOI: 10.1002/MAME.202400104.

128 M. Soheilmoghaddam, H. Adelnia, H. C. Bidsorkhi, G. Sharifzadeh, M. U. Wahit, N. I. Akos and A. A. Yussuf, Development of Ethylene-Vinyl Acetate Composites Reinforced with Graphene Platelets, *Macromol. Mater. Eng.*, 2017, **302**, 1600260, DOI: 10.1002/MAME.201600260.

129 Y. Wang, X. Jia, H. Shi, J. Hao, H. Qu and J. Wang, Graphene Nanoplatelets Hybrid Flame Retardant Containing Ionic Liquid and Ammonium Polyphosphate for Modified Bismaleimide Resin: Excellent Flame Retardancy, Thermal Stability, Water Resistance and Unique Dielectric Properties, *Materials*, 2021, **14**, 6406, DOI: 10.3390/MA14216406.

130 S. Araby, B. Philips, Q. Meng, J. Ma, T. Laoui and C. H. Wang, Recent advances in carbon-based nanomaterials for flame retardant polymers and composites, *Composites, Part B*, 2021, **212**, 108675, DOI: 10.1016/J.COMPOSITESB.2021.108675.

131 S. Sinha Ray and M. Kuruma, Melt-Dripping and Char Formation, *Springer Ser. Mater. Sci.*, 2020, **294**, 69–82, DOI: 10.1007/978-3-030-35491-6_6.

132 P. Yang, H. Wu, F. Yang, J. Yang, R. Wang and Z. Zhu, A novel self-assembled graphene-based flame retardant: Synthesis and flame retardant performance in pla, *Polymers*, 2021, **13**, 4216, DOI: 10.3390/POLYM13234216/S1.

133 J. Yang, S. Nie, Y. Qiao, Y. Liu, Z. Li and G. Cheng, Crystallization and Rheological Properties of the Eco-friendly Composites Based on Poly (lactic acid) and Precipitated Barium Sulfate, *J. Polym. Environ.*, 2019, **27**, 2739–2755, DOI: 10.1007/S10924-019-01557-1.

134 G. Tang, R. Zhang, X. Wang, B. Wang, L. Song, Y. Hu and X. Gong, Enhancement of Flame Retardant Performance of Bio-Based Polylactic Acid Composites with the Incorporation of Aluminum Hypophosphite and Expanded Graphite, *J. Macromol. Sci., Part A:Pure Appl. Chem.*, 2013, **50**, 255–269, DOI: 10.1080/10601325.2013.742835.

135 J. Zhuge, J. Gou and C. Ibeh, Flame resistant performance of nanocomposites coated with exfoliated graphite nanoplatelets/carbon nanofiber hybrid nanopapers, *Fire Mater.*, 2012, **36**, 241–253, DOI: 10.1002/FAM.1104.

136 B. Shen, W. Zhai and W. Zheng, Ultrathin Flexible Graphene Film: An Excellent Thermal Conducting Material with Efficient EMI Shielding, *Adv. Funct. Mater.*, 2014, **24**, 4542–4548, DOI: 10.1002/ADFM.201400079.

137 M. H. Al-Saleh and U. Sundararaj, Electromagnetic interference shielding mechanisms of CNT/polymer composites, *Carbon*, 2009, **47**, 1738–1746, DOI: 10.1016/J.CARBON.2009.02.030.

138 Y. Rong, H. Guo, X. Zhou, W. Wu, W. Zhu, H. Wang, X. Ma, S. Jiang and Q. Sun, Absorption-Dominant Electromagnetic Interference Shielding Materials: from Microstructure to Multi-Scale Assembly, *Adv. Funct. Mater.*, 2025, e06746, DOI: 10.1002/ADFM.202506746.

139 B. Park, S. Hwang, H. Lee, Y. Jung, T. Kim, S. J. Kwon, D. Jung and S. Lee, Absorption-Dominant Electromagnetic Interference (EMI) Shielding across

Multiple mmWave Bands Using Conductive Patterned Magnetic Composite and Double-Walled Carbon Nanotube Film, *Adv. Funct. Mater.*, 2024, **34**, 2406197, DOI: 10.1002/ADFM.202406197.

140 Y. Wu, C. An and Y. Guo, 3D Printed Graphene and Graphene/Polymer Composites for Multifunctional Applications, *Materials*, 2023, **16**, 5681, DOI: 10.3390/ma16165681.